
Bayesian Neural Networks for One-to-Many Mapping in Image Enhancement

Guoxi Huang¹ Nantheera Anantrasirichai¹ Fei Ye² Zipeng Qi³ RuiRui Lin¹ Qirui Yang⁴ David Bull¹

Abstract

In image enhancement tasks, such as low-light and underwater image enhancement, a degraded image can correspond to multiple plausible target images due to dynamic photography conditions, such as variations in illumination. This naturally results in a one-to-many mapping challenge. To address this, we propose a Bayesian Enhancement Model (BEM) that incorporates Bayesian Neural Networks (BNNs) to capture data uncertainty and produce diverse outputs. To achieve real-time inference, we introduce a two-stage approach: Stage I employs a BNN to model the one-to-many mappings in the low-dimensional space, while Stage II refines fine-grained image details using a Deterministic Neural Network (DNN). To accelerate BNN training and convergence, we introduce a dynamic *Momentum Prior*. Extensive experiments on multiple low-light and underwater image enhancement benchmarks demonstrate the superiority of our method over deterministic models. Our code is available at [this link](#).

1. Introduction

In computer vision, image enhancement refers to the process of enhancing the perceptual quality, visibility, and overall appearance of an image, which can involve reducing noise, increasing contrast, sharpening details, or correcting colour imbalances. In image enhancement tasks such as low-light image enhancement (LLIE) and underwater image enhancement (UIE), a common challenge is the *one-to-many mapping* problem, where a single degraded input image can correspond to multiple plausible target images due to dynamic photography conditions, such as variations in lighting, exposure, or other factors. As shown in Figure 1 (left), we observe that existing datasets often exhibit a one-to-many relationship between input and target domains, where identical

or visually similar input images correspond to significantly different targets. An effective image enhancement method should be capable of modelling the one-to-many mapping between inputs and outputs.

Recent advances in deep learning have steered image enhancement towards data-driven approaches, with several models (Peng et al., 2023; Cai et al., 2023) achieving state-of-the-art results by learning mappings between low-quality (LQ) inputs and high-quality (HQ) counterparts using paired datasets. However, the target ambiguity makes deterministic neural networks (DNNs) ill-suited for capturing the variability in these one-to-many image pairs, as depicted in Figure 1 (middle).

In this paper, we use a Bayesian Neural Network (BNN) to probabilistically model the one-to-many mappings between inputs and outputs. Unlike suboptimal deterministic methods, our approach leverages Bayesian inference to sample network weights from a learned posterior distribution, with each sampled set of weights representing a distinct solution. Through multiple sampling processes, the model maps a single input to a distribution of possible outputs, as illustrated in Figure 1 (right). While BNNs have demonstrated promise in capturing uncertainty across various tasks (Kendall & Cipolla, 2016; Kendall et al., 2015; 2018; Pang et al., 2020), their potential for mapping a single input to multiple targets in image enhancement remains largely under-explored. By incorporating Bayesian inference into the enhancement process, our approach captures uncertainty in dynamic, uncontrolled environments, providing a more flexible and robust solution than traditional deterministic models.

However, applying BNNs to image tasks presents significant challenges: The BNN with high-dimensional weight spaces are prone to underfitting (Dusenberry et al., 2020; Tomczak et al., 2021). To mitigate the underfitting problem of BNN, we propose Momentum prior, enabling the faster convergence. Meanwhile, to achieve real-time inference for BNN, we propose a two-stage approach that combines a BNN and a DNN (Sec. 4). Following our approach, we systematically address these challenges, unleashing the potential of BNNs in LLIE and UIE tasks.

As the first work to explore the feasibility of BNNs for image enhancement, we validate our method on the LLIE and UIE tasks where the *one-to-many mapping* problem

¹Visual Information Laboratory, University of Bristol
²University of Electronic Science and Technology of China
³BeiHang University ⁴TianJing University. Correspondence to: Guoxi Huang <guoxi.huang@bristol.ac.uk>, Nantheera Anantrasirichai <n.anantrasirichai@bristol.ac.uk>.

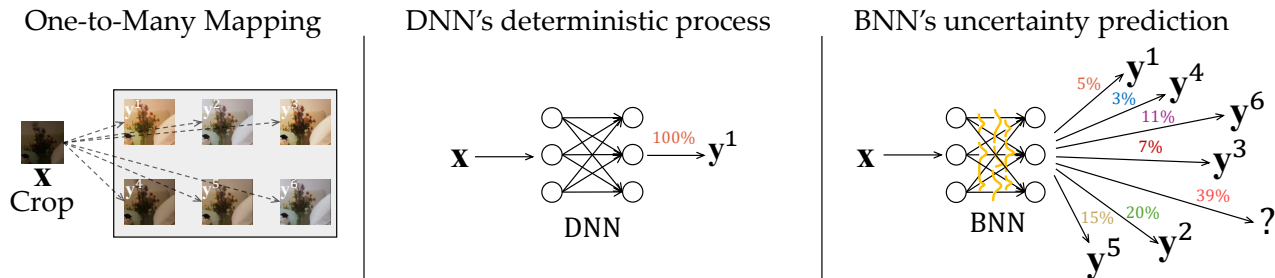


Figure 1: One-to-Many Mapping. The left panel shows an image crop \mathbf{x} associated with multiple targets $\{\mathbf{y}^1, \dots, \mathbf{y}^6\}$. A DNN (middle) can only predict one of the targets. In contrast, a BNN (right) can produce many predictions according to a learned probability distribution.

is particularly pronounced. The main contributions of this paper are summarised as follows:

- We identify the one-to-many mapping between inputs and outputs as a key bottleneck in image enhancement models for LLIE and UIE, and propose the first BNN-based model to address this challenge.
- We propose the *Momentum Prior* to enable the BNN to converge to a better local optimum within the complex, high-dimensional weight space.
- To reduce inference latency in BNNs when generating multiple predictions, we propose a two-stage framework that leverages the complementary strengths of BNN and DNN.

2. Background

2.1. Related Work

Bayesian Deep Learning. BNNs quantify uncertainty by learning distributions over network weights, offering robust predictions (Neal, 2012). Variational Inference (VI) is a common method for approximating these distributions (Graves, 2011; Blundell et al., 2015). Gal & Ghahramani (2016) simplify the implementation of BNNs by interpreting dropout as an approximate Bayesian inference method. Recent advancements show that adding uncertainty only to the final layer can efficiently approximate a full BNN (Harrison et al., 2024). Another line of approaches, such as Krishnan et al. (2020), explored the use of empirical Bayes to specify weight priors in BNNs to enhance the model’s adaptability to diverse datasets. These BNN approaches have shown promise across a range of vision applications, including camera relocalisation (Kendall & Cipolla, 2016), semantic and instance segmentation (Kendall et al., 2015; 2018). Despite these advances, BNNs remain underutilised in image enhancement tasks.

Probabilistic Models in Image Enhancement. Several works have utilised probabilistic models to address different aspects of image enhancement. Jiang et al. (2021) employed GANs to capture features for LLIE, while Fabbri

et al. (2018) leveraged CycleGAN (Zhu et al., 2017) to generate synthetic paired datasets, addressing data scarcity in UIE. FUnIE-GAN (Islam et al., 2020) further demonstrated effectiveness in both paired and unpaired UIE training. Anantrasirichai & Bull (2021) applied unpaired learning for LLIE when the scene conditions are known. Wang et al. (2022) applied normalising flow-based methods to reduce residual noise in LLIE predictions. However, its invertibility constraint limits model complexity. Zhou et al. (2024) mitigated this by integrating normalising flows with codebook techniques, introducing latent normalising flows. Diffusion Models (DMs) have been widely adopted for enhancement tasks (Hou et al., 2024; Tang et al., 2023). While DMs inherently address one-to-many mappings, their high latency for generating a single sample makes producing multiple candidates impractical due to prohibitive delays.

2.2. Preliminary

In image enhancement, the output of a neural network can be interpreted as the conditional probability distribution of the target image, $\mathbf{y} \in \mathcal{Y}$, given the degraded input image $\mathbf{x} \in \mathcal{X}$, and the network’s weights \mathbf{w} : $P(\mathbf{y}|\mathbf{x}, \mathbf{w})$. Assuming the prediction errors follow a Gaussian distribution, the conditional probability density function (PDF) of the target image \mathbf{y} can be modelled as a multivariate Gaussian, where the mean is given by the neural network output $F(\mathbf{x}; \mathbf{w})$:

$$P(\mathbf{y}|\mathbf{x}, \mathbf{w}) = \mathcal{N}(\mathbf{y}|F(\mathbf{x}; \mathbf{w}), \text{diag}(\boldsymbol{\sigma}^2)). \quad (1)$$

The network weights \mathbf{w} can be learned through maximum likelihood estimation (MLE). Given a dataset of image pairs $\{\mathbf{x}^i, \mathbf{y}^i\}_{i=1}^N$, the MLE estimate \mathbf{w}^{MLE} is computed by maximising the log-likelihood of the observed data:

$$\mathbf{w}^{\text{MLE}} = \underset{\mathbf{w}}{\text{argmax}} \sum_{i=1}^N \log P(\mathbf{y}^i|\mathbf{x}^i, \mathbf{w}). \quad (2)$$

By optimising such an objective function in Equation (2), the network $F_{\mathbf{w}}$ learns an injective function, $F_{\mathbf{w}} : \mathcal{X} \rightarrow \mathcal{Y}$. The deterministic nature of such a mapping implies that when $\mathbf{y}^i \neq \mathbf{y}^j$, the condition $\mathbf{x}^i \neq \mathbf{x}^j$ must hold. We argue

that this deterministic process is inadequate in cases where one input corresponds to multiple plausible targets.

3. Modelling the one-to-many mapping

3.1. Bayesian Enhancement Models (BEMs)

We introduce uncertainty into the network weights \mathbf{w} through Bayesian estimation, thus obtaining a posterior distribution over the weight, $\mathbf{w} \sim P(\mathbf{w}|\mathbf{y}, \mathbf{x})$. During inference, weights are sampled from this distribution. The posterior distribution over the weights is expressed as:

$$P(\mathbf{w}|\mathbf{y}, \mathbf{x}) = \frac{P(\mathbf{y}|\mathbf{x}, \mathbf{w})P(\mathbf{w})}{P(\mathbf{y}|\mathbf{x})}, \quad (3)$$

where $P(\mathbf{y} | \mathbf{x}, \mathbf{w})$ is the likelihood of observing \mathbf{y} given the input \mathbf{x} and weights \mathbf{w} , $P(\mathbf{w})$ denotes the prior distribution of the weights, and $P(\mathbf{y} | \mathbf{x})$ is the marginal likelihood.

Unfortunately, for any neural networks the posterior in Equation (3) cannot be calculated analytically. This makes it impractical to directly sample weights from the true posterior distribution. Instead, we can leverage variational inference (VI) to approximate $P(\mathbf{w}|\mathbf{y}, \mathbf{x})$ with a more tractable distribution $q(\mathbf{w}|\boldsymbol{\theta})$. Such that, we can draw samples of weights \mathbf{w} from the distribution $q(\mathbf{w}|\boldsymbol{\theta})$. As suggested by (Hinton & Van Camp, 1993; Graves, 2011; Blundell et al., 2015), the variational approximation is fitted by minimising their Kullback-Leibler (KL) divergence:

$$\begin{aligned} \boldsymbol{\theta}^* &= \underset{\boldsymbol{\theta}}{\operatorname{argmin}} \operatorname{KL} [q(\mathbf{w}|\boldsymbol{\theta}) \| P(\mathbf{w}|\mathbf{y}, \mathbf{x})] \\ &= \underset{\boldsymbol{\theta}}{\operatorname{argmin}} \int q(\mathbf{w}|\boldsymbol{\theta}) \log \frac{q(\mathbf{w}|\boldsymbol{\theta})}{P(\mathbf{w})P(\mathbf{y}|\mathbf{x}, \mathbf{w})} d\mathbf{w} \\ &= \underset{\boldsymbol{\theta}}{\operatorname{argmin}} -\mathbb{E}_{q(\mathbf{w}|\boldsymbol{\theta})} [\log P(\mathbf{y}|\mathbf{x}, \mathbf{w})] \\ &\quad + \operatorname{KL} [q(\mathbf{w}|\boldsymbol{\theta}) \| P(\mathbf{w})]. \end{aligned} \quad (4)$$

We define the resulting cost function from Equation (4) as:

$$\begin{aligned} \mathcal{L}(\mathbf{x}, \mathbf{y}, \boldsymbol{\theta}) &= \underbrace{-\mathbb{E}_{q(\mathbf{w}|\boldsymbol{\theta})} [\log P(\mathbf{y}|\mathbf{x}, \mathbf{w})]}_{\text{data-dependent term}} \\ &\quad + \underbrace{\operatorname{KL} [q(\mathbf{w}|\boldsymbol{\theta}) \| P(\mathbf{w})]}_{\text{prior matching term}}. \end{aligned} \quad (5)$$

The loss function $\mathcal{L}(\mathbf{x}, \mathbf{y}, \boldsymbol{\theta})$ in Equation (5), also known as the variational free energy, consists of two components: the prior matching term and the data-dependent term. The prior matching term can be approximated using the Monte Carlo method or computed analytically if a closed-form solution exists. The data-dependent term is equivalent to minimising the mean squared error between the input-output pairs in the training data. To optimise $\mathcal{L}(\mathbf{x}, \mathbf{y}, \boldsymbol{\theta})$, the prior distribution $P(\mathbf{w})$ must be defined. In Sec. 3.2, we define $P(\mathbf{w})$ as a dynamic prior, which can accelerate the convergence of BNN training.

3.2. Momentum Prior

In our preliminary work, a low convergence is encountered when using naive Gaussian (e.g., $\mathcal{N}(\mathbf{0}, \mathbf{I})$) or empirical Bayes priors. To address this, we propose *Momentum Prior*, a simple yet effective strategy that uses an exponential moving average to stabilise training by smoothing parameter updates and promoting convergence to better local optima. Suppose that the variational posterior $q(\mathbf{w}|\boldsymbol{\theta})$ is a diagonal Gaussian, then the variational posterior parameters are $\boldsymbol{\theta} = (\boldsymbol{\mu}, \boldsymbol{\sigma})$. A posterior sample of the weights \mathbf{w} is obtained via the reparameterisation trick (Kingma, 2014).

$$\mathbf{w} = \boldsymbol{\mu} + \boldsymbol{\sigma} \circ \boldsymbol{\epsilon} \quad \text{with } \boldsymbol{\epsilon} \sim \mathcal{N}(\mathbf{0}, \mathbf{I}). \quad (6)$$

Having liberated our algorithm from the confines of fixed priors, we propose a dynamic prior by updating the prior's parameters to the exponential moving average (EMA) of the variational posterior parameters. Specifically, for the prior distribution $P(\mathbf{w}) = \mathcal{N}(\mathbf{w}; \boldsymbol{\mu}_t^{\text{EMA}}, \boldsymbol{\sigma}_t^{\text{EMA}^2} \mathbf{I})$, the parameters are updated at each minibatch training step t over the training period $[0, 1, 2, \dots, T]$ as follows:

$$\begin{aligned} \boldsymbol{\mu}_0^{\text{EMA}} &= \mathbf{0}, \quad \boldsymbol{\sigma}_0^{\text{EMA}} = \sigma^o \mathbf{1}, \\ \boldsymbol{\mu}_t^{\text{EMA}} &= \beta \boldsymbol{\mu}_{t-1}^{\text{EMA}} + (1 - \beta) \boldsymbol{\mu}_t, \quad t = 1 \dots T, \\ \boldsymbol{\sigma}_t^{\text{EMA}} &= \beta \boldsymbol{\sigma}_{t-1}^{\text{EMA}} + (1 - \beta) \boldsymbol{\sigma}_t, \quad t = 1 \dots T, \end{aligned} \quad (7)$$

where $\boldsymbol{\mu}_t$ and $\boldsymbol{\sigma}_t$ represent the mean and variance from the variational posterior $q(\mathbf{w}|\boldsymbol{\theta})$ at training step t , σ^o is a scalar controlling the magnitude of initial variance in the prior distribution $P(\mathbf{w})$, and β denotes the EMA decay rate. Thereafter, for minibatch optimisation with M image pairs, we update $\boldsymbol{\theta} = (\boldsymbol{\mu}, \boldsymbol{\sigma})$ at step t by minimising minibatch loss $\mathcal{L}^{\text{mini}}(\mathbf{x}, \mathbf{y})$, reformulated from Equation (5) as:

$$\begin{aligned} \mathcal{L}^{\text{mini}}(\mathbf{x}, \mathbf{y}, \boldsymbol{\theta}) &= \underbrace{-\mathbb{E}_{q(\mathbf{w}|\boldsymbol{\theta})} [\log P(\mathbf{y}|\mathbf{x}, \mathbf{w})]}_{\text{data-dependent term}} \\ &\quad + \underbrace{\frac{1}{M} \operatorname{KL} [q(\mathbf{w}|\boldsymbol{\theta}) \| P(\mathbf{w})]}_{\text{prior matching term}}, \\ &= \frac{1}{M} \left[\underbrace{\sum_i^M \mathbb{E}_{\mathbf{w} \sim q(\mathbf{w}|\boldsymbol{\theta})} \|F(\mathbf{x}^i; \mathbf{w}) - \mathbf{y}^i\|_2^2}_{\text{data-dependent term}} \right. \\ &\quad \left. + \log \frac{\boldsymbol{\sigma}_t^{\text{EMA}}}{\boldsymbol{\sigma}} + \frac{\boldsymbol{\sigma}^2 + (\boldsymbol{\mu} - \boldsymbol{\mu}_t^{\text{EMA}})^2}{2\boldsymbol{\sigma}_t^{\text{EMA}^2}} - \frac{1}{2} \right], \end{aligned} \quad (8)$$

where the prior matching term is expressed as the analytical solution of $\operatorname{KL} [q(\mathbf{w}|\boldsymbol{\theta}) \| P(\mathbf{w})]$. An analysis of Momentum prior compared to other fixed priors is provided in Appendix B.

After optimising the variational posterior parameters $\boldsymbol{\theta}^*$ using Equation (8), the BNN generates multiple distinct

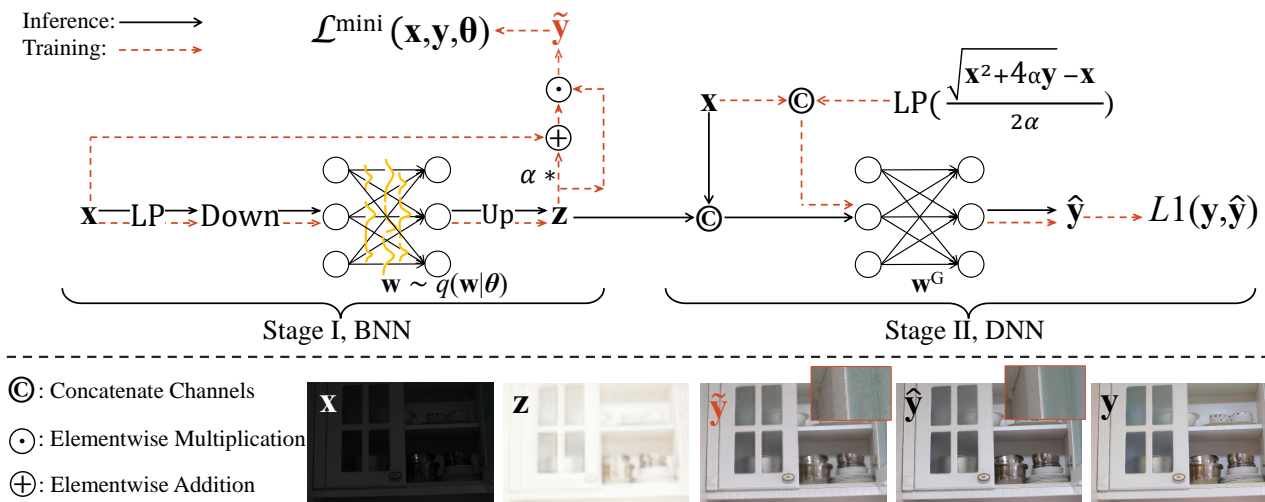


Figure 2: The two-stage pipeline. In Stage I, the BNN with weights $\mathbf{w} \sim q(\mathbf{w}|\theta)$ is trained by minimising the minibatch loss $\mathcal{L}^{\text{mini}}$ in Equation (8). In Stage II, the DNN with weights \mathbf{w}^G is trained by minimising the L1 loss, $L1(\mathbf{y}, \hat{\mathbf{y}})$. The inference process is denoted by \rightarrow , while the training process for each stage is indicated by \dashrightarrow .

predictions $\{\hat{\mathbf{y}}_1, \hat{\mathbf{y}}_2, \dots, \hat{\mathbf{y}}_K\}$ by sampling different weights \mathbf{w} from the variational posterior distribution $q(\mathbf{w}|\theta)$ during each forward pass. The inference process of the BNN is detailed in Sec. 5.1.

4. BNN+DNN: A two-stage approach

In a BNN, producing multiple high-resolution predictions can incur a high computational footprint. However, in most cases, we are only interested in the highest-quality prediction among $\{\hat{\mathbf{y}}_1, \hat{\mathbf{y}}_2, \dots, \hat{\mathbf{y}}_K\}$.

To achieve real-time inference, we design a two-stage BNN+DNN framework, illustrated in Figure 2. The first stage leverages a BNN to model the one-to-many mapping in the low-dimensional coarse information, while the second stage employs a DNN to refine high-frequency details in the original high-dimensional space. This coarse-to-fine architecture is motivated by our observation that the one-to-many mapping stems from uncertainties in image illumination and colour variations (see Sec. 6.3), which can be effectively represented in a low-dimensional space, as also noted by Xu et al. (2020). Consequently, the low-dimensional coarse information serves as a proxy to identify the highest-quality prediction among $\{\mathbf{y}_k\}_{k=1}^K$, eliminating the need to produce all predictions directly.

4.1. The Framework

In Stage I, we employ low-pass filtering¹ followed by downsampling to map the input’s coarse information into a lower-dimensional space, $\text{Down}(\text{LP}(\mathbf{x}), r)$, where r denotes the scaling factor and LP represents a low-pass filter

¹Applying a low-pass filter before downsampling can avoid spatial aliasing in the output.

implemented via FFT. Subsequently, a BNN models the uncertainty in the low-dimensional coarse input information. The forward process of Stage I can be expressed as:

$$\mathbf{z} = \text{Up}(F(\text{Down}(\text{LP}(\mathbf{x}), r); \mathbf{w})), \quad \mathbf{w} \sim q(\mathbf{w} | \theta), \quad (9)$$

where $\text{Up}(\cdot)$ is the bilinear upsampling operation for dimensionality matching. For a single input image \mathbf{x} , multiple distinct \mathbf{z} values can be generated by running the forward function multiple times. From Figure 2, we can observe that \mathbf{z} approximates the enhanced illumination condition. The first-stage prediction of the target \mathbf{y} , denoted as $\tilde{\mathbf{y}}$, is obtained by combining the input \mathbf{x} with the coarse prediction \mathbf{z} :

$$\tilde{\mathbf{y}} = (\mathbf{x} + \alpha\mathbf{z}) * \mathbf{z}, \quad (10)$$

where α is a small scalar. Compared to simpler formulations, such as $\mathbf{x} + \mathbf{z}$ or $\mathbf{x} * \mathbf{z}$, Equation (10) reduces the risk of blurring fine textures or amplifying noise in \mathbf{x} . Furthermore, $\tilde{\mathbf{y}}$ plays a key role in the ranking-based inference in Sec. 5.1.

In Stage II, we employ a DNN G to enhance the fine-grained details in the input. The forward process can be expressed as:

$$\hat{\mathbf{y}} = G([\mathbf{x}, \mathbf{z}]; \mathbf{w}^G), \quad (11)$$

where \mathbf{w}^G represents the weights of the second-stage model, $[\cdot, \cdot]$ denotes the concatenation operation along the channel dimension. When training the second-stage DNN, we replace the prediction of coarse information \mathbf{z} with its ground truth, $\text{LP}\left(\frac{\sqrt{\mathbf{x}^2 + 4\alpha\mathbf{y}} - \mathbf{x}}{2\alpha}\right)$. This strategy avoids the problem where many predictions from the first-stage BNN are regressed into a single output by the second-stage DNN.

4.2. The Backbone

For both the first- and second-stage models, we adopt the same backbone network but use different input and output layers. In the first stage, we construct a BNN by converting all layers in the backbone to their Bayesian counterparts via Equation (6). We observe that converting only the normalisation layers can also simulate a BNN, but it results in reduced diversity in the output. Additionally, using Instance Normalisation (Ulyanov, 2016) to the BNN, can better capture high-contrast local illumination. The backbone follows an encoder-decoder UNet design. For the basic blocks, we consider both Transformers (Vaswani et al., 2017) and Mamba (Gu & Dao, 2023), demonstrating the broad applicability of our methods across the two primary backbone architectures. We provide more details in Appendix A.

5. Inference

Algorithm 1 Inference

Require: Input \mathbf{x} , BNN F , DNN G

for $k = 1$ to K **do**

$\mathbf{w}_k \leftarrow \boldsymbol{\mu} + \boldsymbol{\sigma} \circ \boldsymbol{\epsilon}_k$, where $\boldsymbol{\epsilon}_k \sim \mathcal{N}(\mathbf{0}, \mathbf{I})$

$\mathbf{z}_k \leftarrow F(\text{Down}(\text{LP}(\mathbf{x}), r); \mathbf{w}_k)$ *Stage I*

end for

if Mode = *Monte Carlo* **then**

$\mathbf{z}^* \leftarrow \frac{\mathbf{z}_1 + \mathbf{z}_2 + \dots + \mathbf{z}_K}{K}$

else

$\mathbf{z}^* \leftarrow \underset{\mathbf{z}_k \in \{\mathbf{z}_1, \mathbf{z}_2, \dots, \mathbf{z}_K\}}{\text{argmax}} \text{IQA}((\mathbf{x} + \alpha \mathbf{z}_k) * \mathbf{z}_k)$

end if

$\hat{\mathbf{y}} \leftarrow G([\mathbf{x}, \text{Up}(\mathbf{z}^*); \mathbf{w}^G)$ *Stage II*

Ensure: $\hat{\mathbf{y}}$

5.1. Predictions Under Uncertainty

We describe two types of inference: Monte Carlo (MC) prediction and ranking-based prediction. As detailed in Algorithms 1, both types of inference use the first-stage BNN to generate K predictions of the coarse information, $\{\mathbf{z}_k\}_{k=1}^K$, which can be implemented in parallel.

Thereafter, for Monte Carlo simulation, we average $\{\mathbf{z}_1, \mathbf{z}_2, \dots, \mathbf{z}_K\}$ to obtain \mathbf{z}^* , which is then processed by the second-stage DNN to produce the final prediction $\hat{\mathbf{y}}$. By modelling uncertainty, MC prediction demonstrates high robustness across diverse scenarios. For ranking-based prediction, we use an image quality assessment metric, IQA(\cdot), to score the K coarse predictions $\{\hat{\mathbf{y}}_k\}_{k=1}^K$ from Equation (10). The coarse prediction with the highest score is refined in the second stage and used as the final output.

For the IQA metric, we primarily employ CLIP-IQA (Wang et al., 2023), as it not only supports parallel quality evaluation of multiple \mathbf{z}_k , but also allows our BEM to produce enhanced images tailored to specific image quality

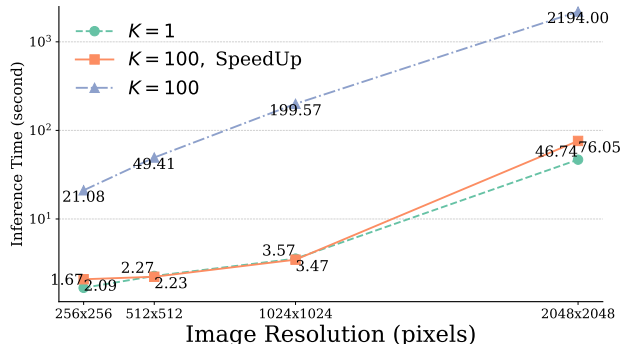


Figure 3: Inference speed before and after acceleration. The model runs on an Nvidia RTX 4090.

requirements through diverse text prompts and their combinations. We denote the BEM using CLIP as BEM_{CLIP} and the BEM using the MC method as BEM_{MC} . Additionally, we can also employ other no-reference IQA metrics, such as NIQE (Mittal et al., 2012), UIQM (Panetta et al., 2015), and UCIQE (Yang & Sowmya, 2015).

5.2. Speeding Up

Algorithm 1 eliminates the need to produce multiple redundant outputs, significantly accelerating inference speed. In Figure 3, we analyse the inference latency before and after applying Algorithm 1. With the acceleration provided by Algorithm 1 and our two-stage framework, our BEM achieves a similar inference speed to a single forward pass. This indicates that the inference speed bottleneck is no longer constrained by the multiple forward passes of the BNN but is instead primarily determined by the backbone’s latency. As our method is compatible with most backbone architectures, the inference speed can be further improved by incorporating future lightweight backbone techniques.

6. Experiments

Datasets. For LLIE, we evaluate our method on the paired LOL-v1 (Wei et al., 2018) and LOL-v2 (real and synthetic subsets) (Yang et al., 2021) datasets, as well as the unpaired LIME (Guo et al., 2016), NPE (Wang et al., 2013), MEF (Ma et al., 2015), DICM (Lee et al., 2013), and VV (Vonikakis et al., 2018) datasets. For UIE, we evaluate our method on the paired UIEB-R90 (Li et al., 2019a) dataset, along with unpaired datasets including UIEB-C60, U45 (Li et al., 2019b), and UCCS (Liu et al., 2020).

Settings. All models are trained using the Adam optimiser, with an initial learning rate of 2×10^{-4} , decayed to 10^{-6} following a cosine annealing schedule. The first-stage model is trained for 300K iterations, while the second-stage model is trained for 150K iterations on inputs of size 128×128 . The batch size M is set to 8, and the downscale factor r in Equation (9) is set to $\frac{1}{16}$. Unless stated otherwise, K is set to 25, σ^o in Equation (7) is set to 0.05, and the adopted

Table 1: Full-reference evaluation on LOL-v1 and v2. The best results are in **bold**, while the second-best are underlined. Results in grey represent the upper bound performance of BEM, which is not directly comparable to the other results.

| Method | LOL-v1 | | | LOL-v2-real | | | LOL-v2-syn | | |
|--|-----------------|-----------------|--------------------|-----------------|-----------------|--------------------|-----------------|-----------------|--------------------|
| | PSNR \uparrow | SSIM \uparrow | LPIPS \downarrow | PSNR \uparrow | SSIM \uparrow | LPIPS \downarrow | PSNR \uparrow | SSIM \uparrow | LPIPS \downarrow |
| KinD (Zhang et al., 2019) | 19.66 | 0.820 | 0.156 | 18.06 | 0.825 | 0.151 | 17.41 | 0.806 | 0.255 |
| Restormer (Zamir et al., 2022) | 22.43 | 0.823 | 0.147 | 18.60 | 0.789 | 0.232 | 21.41 | 0.830 | 0.144 |
| SNR-Net (Xu et al., 2022) | 24.61 | 0.842 | 0.151 | 21.48 | 0.849 | 0.157 | 24.14 | 0.928 | 0.056 |
| RetinexFormer (Cai et al., 2023) | 25.16 | 0.845 | 0.131 | 22.80 | 0.840 | 0.171 | 25.67 | 0.930 | 0.059 |
| RetinexMamba (Bai et al., 2024) | 24.03 | 0.827 | 0.146 | 22.45 | 0.844 | 0.174 | 25.89 | 0.935 | 0.054 |
| LLFlow (Wang et al., 2022) | 25.13 | 0.872 | 0.117 | 26.20 | 0.888 | 0.137 | 24.81 | 0.919 | 0.067 |
| GlobalDiff (Hou et al., 2024) | 27.84 | 0.877 | 0.091 | 28.82 | 0.895 | 0.095 | 28.67 | 0.944 | 0.047 |
| GLARE (Zhou et al., 2024) | 27.35 | 0.883 | 0.083 | 28.98 | 0.905 | 0.097 | 29.84 | 0.958 | - |
| Transformer BEM _{UB} (ours) | 28.24 | 0.881 | 0.077 | 32.54 | 0.917 | 0.072 | 32.36 | 0.962 | 0.030 |
| Transformer BEM _{MC} (ours) | 27.22 | 0.879 | 0.075 | <u>30.86</u> | 0.905 | <u>0.069</u> | 30.21 | 0.944 | 0.035 |
| Mamba BEM _{UB} (ours) | 28.80 | 0.884 | 0.069 | 32.66 | 0.915 | 0.060 | 32.95 | 0.964 | 0.026 |
| Mamba BEM _{MC} (ours) | <u>28.30</u> | 0.881 | <u>0.072</u> | 31.41 | 0.912 | 0.064 | <u>30.58</u> | <u>0.958</u> | <u>0.033</u> |
| Mamba BEM _{CLIP} (ours) | 28.43 | <u>0.882</u> | 0.071 | 30.01 | <u>0.910</u> | 0.076 | 31.51 | 0.961 | 0.030 |

Table 2: No-reference evaluation on LIME, NPE, MEF, DICM and VV, in terms of NIQE \downarrow .

| Method | DICM | LIME | MEF | NPE | VV |
|----------------------------|-------------|-------------|-------------|-------------|-------------|
| KinD (Zhang et al., 2019) | 5.15 | 5.03 | 5.47 | 4.98 | 4.30 |
| ZeroDCE (Guo et al., 2020) | 4.58 | 5.82 | 4.93 | 4.53 | 4.81 |
| RUAS (Liu et al., 2021) | 5.21 | 4.26 | 3.83 | 5.53 | 4.29 |
| LLFlow (Wang et al., 2022) | 4.06 | 4.59 | 4.70 | 4.67 | 4.04 |
| PairLIE (Fu et al., 2023b) | 4.03 | 4.58 | 4.06 | 4.18 | 3.57 |
| RFR (Fu et al., 2023a) | 3.75 | <u>3.81</u> | 3.92 | 4.13 | - |
| GLARE (Zhou et al., 2024) | <u>3.61</u> | 4.52 | 3.66 | 4.19 | - |
| CIDNet (Feng et al., 2024) | 3.79 | 4.13 | 3.56 | <u>3.74</u> | 3.21 |
| BEM _{MC} (ours) | 3.77 | 3.94 | <u>3.22</u> | 3.85 | <u>2.95</u> |
| BEM (ours) | 3.55 | 3.56 | 3.14 | 3.72 | 2.91 |

backbone architecture is Mamba. The default text prompt for CLIP-IQA is “A bright, natural, and good quality photo.”

6.1. Full-Reference Evaluation

We present quantitative comparisons with state-of-the-art (SOTA) methods for LLIE on the LOL-v1 and LOL-v2 datasets (Table 1) and for UIE on the UIEB-R90 dataset (Table 3, left). Our BEM outperforms most previous methods across all metrics. Furthermore, the Mamba-based BEM demonstrates better performance than its Transformer counterpart, which can be attributed to Mamba’s superior global context modelling capability. Previous methods struggle to maintain high perceptual quality (measured by LPIPS) while ensuring pixel-level accuracy. However, our BEM excels in both, delivering higher SSIM and lower LPIPS. This superior performance across both LLIE and UIE tasks highlights the effectiveness and versatility of BEM. Additionally, we provide BEM’s performance upper bound (BEM_{UB}) by calculating the full-reference metrics for its 100 outputs and reporting the highest values. This upper bound serves as a baseline for future one-to-many modelling methods.

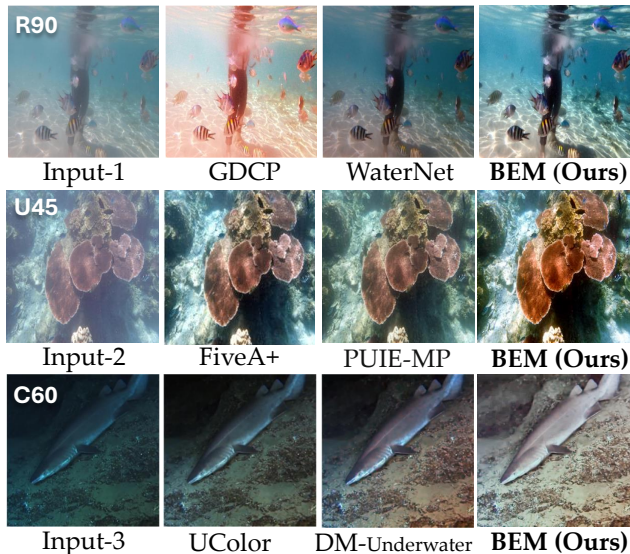


Figure 4: Visual comparisons on the R90, C60 and U45 datasets. Best viewed when zoomed in.

6.2. No-Reference Evaluation

For LLIE, we perform no-reference evaluations on five unpaired datasets, as detailed in Table 2. Alongside CLIP-IQA, we use the negative of NIQE for IQA(\cdot) in Algorithm 1, as it has been shown to identify high-quality (HQ) predictions for LLIE (Jiang et al., 2021). From the visualisation of multiple BEM outputs in Figure 5 (bottom right), outputs with lower NIQE values exhibit more natural illumination while avoiding overexposure. Accordingly, the very low NIQE values achieved by our method across five real-world datasets highlight its superior image enhancement capability.

Similarly, for no-reference evaluation on UIE, we also instantiate IQA(\cdot) as the UIQM metric and evaluate our

Table 3: Full-reference evaluation (left) on R90, and no-reference evaluations (right) on C60, U45, and UCCS. Results in grey represent the upper bound performance of BEM, which is not directly comparable to the other results.

| Method | UIEB-R90 | | UIEB-C60 | | U45 | | UCCS | |
|--------------------------------|-----------------|-----------------|-----------------|------------------|-----------------|------------------|-----------------|------------------|
| | PSNR \uparrow | SSIM \uparrow | UIQM \uparrow | UCIQE \uparrow | UIQM \uparrow | UCIQE \uparrow | UIQM \uparrow | UCIQE \uparrow |
| WaterNet (Li et al., 2019a) | 21.04 | 0.860 | 2.399 | 0.591 | - | - | 2.275 | 0.556 |
| Ucolor (Li et al., 2021) | 20.13 | 0.877 | 2.482 | 0.553 | 3.148 | 0.586 | 3.019 | 0.550 |
| PUIE-MP (Fu et al., 2022) | 21.05 | 0.854 | 2.524 | 0.561 | 3.169 | 0.569 | 2.758 | 0.489 |
| Restormer (Zamir et al., 2022) | 23.82 | 0.903 | 2.688 | 0.572 | 3.097 | 0.600 | 2.981 | 0.542 |
| CECF (Cong et al., 2024) | 21.82 | 0.894 | - | - | - | - | - | - |
| FUnIEGAN (Islam et al., 2020) | 19.12 | 0.832 | 2.867 | 0.556 | 2.495 | 0.545 | 3.095 | 0.529 |
| PUGAN (Cong et al., 2023) | 22.65 | 0.902 | 2.652 | 0.566 | - | - | 2.977 | 0.536 |
| U-Shape (Peng et al., 2023) | 20.39 | 0.803 | 2.730 | 0.560 | 3.151 | 0.592 | - | - |
| Semi-UIR (Huang et al., 2023b) | 22.79 | 0.909 | 2.667 | <u>0.574</u> | 3.185 | 0.606 | 3.079 | 0.554 |
| WFI2-Net (Zhao et al., 2024) | 23.86 | 0.873 | - | - | 3.181 | <u>0.619</u> | - | - |
| BEM _{CLIP} (ours) | <u>24.36</u> | <u>0.921</u> | <u>2.885</u> | 0.554 | <u>3.266</u> | 0.608 | <u>3.115</u> | <u>0.558</u> |
| BEM (ours) | 25.62 | 0.940 | 2.931 | 0.567 | 3.406 | 0.620 | 3.224 | 0.561 |

Full-Reference Metric: PSNR



No-Reference Metric:

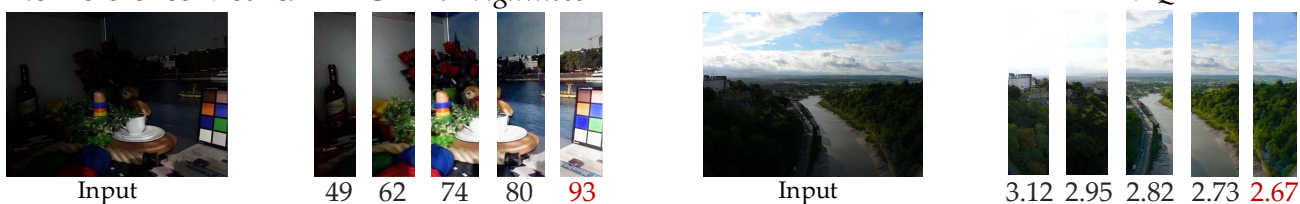


Figure 5: Visualisation of the one-to-many mapping from input to outputs. The predictions are sorted by three metrics: PSNR, CLIP-IQA, and NIQE, which reflect different aspects of image quality. Zoom in for more details on the variations in predictions across these metrics.

method on the C60, U45, and UCCS test sets. As shown in Table 3 (right), BEM achieves the best or comparable results across all three unpaired UIE datasets. To demonstrate that BEM with the UIQM metric can produce high-quality enhanced images, we visually compare the outputs with other SOTA UIE methods, including FiveA+ (Jiang et al., 2023), PUIE (Fu et al., 2022), UColor (Li et al., 2021) and DM-Underwater (Tang et al., 2023). As depicted in the first and second rows of Figure 4, our BEM achieves superior removal of underwater turbidity compared to other methods. These results, spanning two distinct tasks and multiple datasets, highlight the superiority of our BEM in real-world image enhancement without ground truth.

6.3. Uncertainty Maps

The one-to-many mapping arises from uncertainties in image illumination and colour variations. To illustrate this, we present the uncertainty map in Figure 6, computed as the

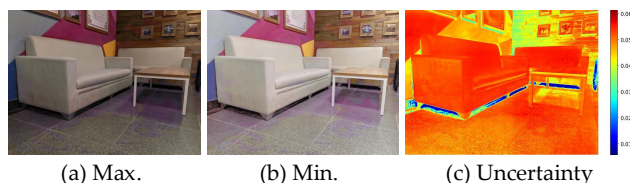


Figure 6: Visualisation of the predictions with the highest (a) and lowest PSNR (b), and the uncertainty map (c).

pixel-wise standard deviation across 500 predictions. The uncertainty map reveals a structured distribution, with shadowed regions exhibiting lower uncertainty and illuminated areas showing higher uncertainty. Additional statistics on predictive uncertainty are provided in Appendix C.

6.4. Visual Analysis

In Figure 5, we visualise the one-to-many mappings from input to outputs modelled by our BEM. These predictions exhibit diverse visual characteristics, capturing plausible

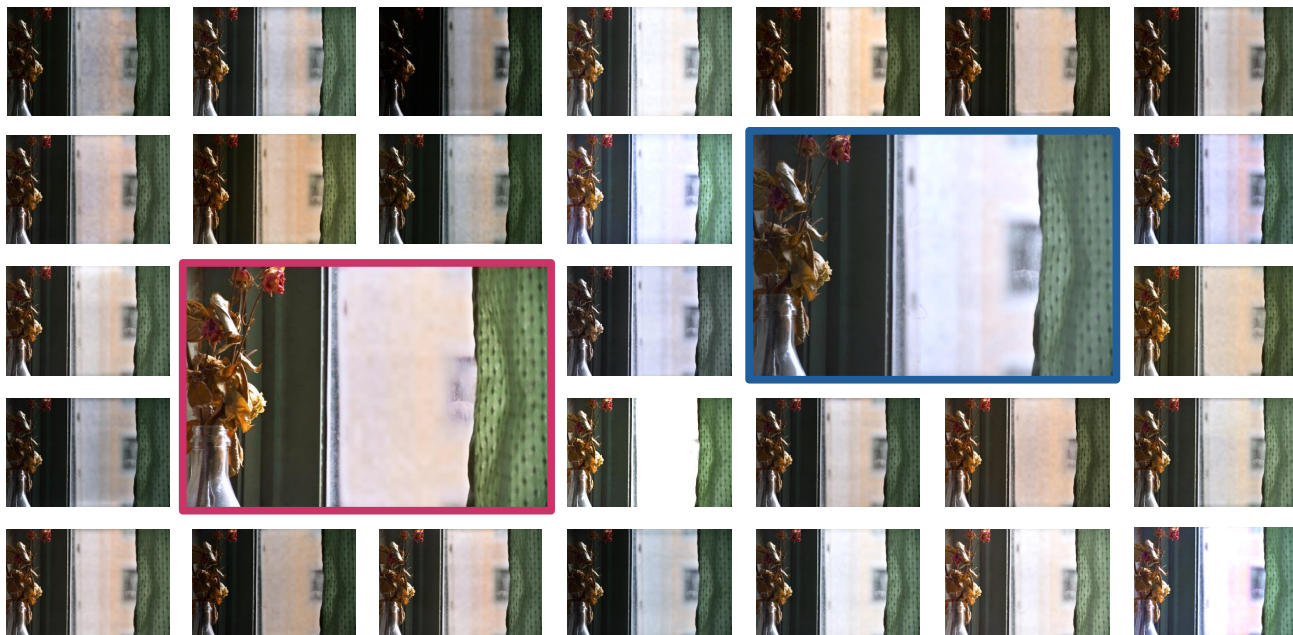


Figure 7: Visualisation of BEM predictions. The pink box (\square) highlights the output selected by CLIP-IQA (“Brightness”, “Natural”, “Quality”), while the blue box (\square) highlights the MC prediction. The input is from LSRW (Hai et al., 2023).

interpretations of the scene under different lighting scenarios. The second row of Figure 5 highlights the use of no-reference metrics such as CLIP-IQA and NIQE. For CLIP-IQA, the ranking reflects how well each output aligns with the semantic understanding of brightness captured by CLIP (Radford et al., 2021). Similarly, for NIQE, we observe how the outputs are ranked in terms of perceived naturalness. Additional qualitative comparisons with other methods are provided in Appendix D.

In Figure 7, we visualise the prediction selected by CLIP-IQA, the MC prediction, and other output candidates. Since the MC prediction represents the probabilistic mean of the training data, it tends to present unnatural illumination, when low-quality ground truth is present in the training set (*i.e.*, label noise). Although the MC output avoids the worst results due to the averaging effect, it could still fail to meet aesthetic expectations. In contrast, CLIP-IQA achieves aesthetically superior results without requiring data cleaning, making it particularly effective for tasks such as UIE and LLIE, where label noise is significant. More analysis for label noise are provided in Appendix C.2 and C.3.

6.5. Magnitude of Uncertainty

The performance improvements of our BEM primarily stem from its ability to effectively model the one-to-many mapping using BNNs. To support this claim, we evaluate the influence of the variance in the variational posterior on model performance. As shown in Figure 8, except for BEM with $\sigma^\circ = 0.0001$, all other BEM instances outperform the DNN

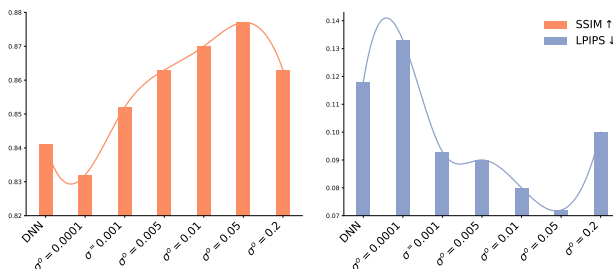


Figure 8: Effect of initial variance values (*i.e.*, σ° in Eq. 7) on model performance. The data is obtained by evaluating single-stage models with $K = 200$ on LOL-v1. “DNN” denotes the deterministic baseline model.

with the same backbone.

7. Conclusion

In this paper, we propose a BNN-based method to address the one-to-many challenge in image enhancement, which is identified as a key limitation in previous data-driven models. To facilitate efficient training of BNNs, we proposed a *Momentum Prior* that dynamically refines the prior distribution during training, enhancing convergence and performance. To achieve real-time inference speed, our two-stage framework integrates the strengths of BNNs and DNNs, yielding a flexible yet computationally efficient model. Extensive experiments on various image enhancement benchmarks demonstrate significant performance gains over state-of-the-art models, showcasing the potential of BNNs in handling the inherent ambiguities of image enhancement tasks.

Acknowledgements

This work was supported by the UKRI MyWorld Strength in Places Program (SIPF0006/1) and the EPSRC ECR International Collaboration Grants (EP/Y002490/1).

Impact Statement

This paper presents work whose goal is to advance the field of Machine Learning. There are many potential societal consequences of our work, none which we feel must be specifically highlighted here.

References

- Anantrasirichai, N. and Bull, D. Contextual colorization and denoising for low-light ultra high resolution sequences. In *2021 IEEE International Conference on Image Processing (ICIP)*, pp. 1614–1618. IEEE, 2021.
- Ashukha, A., Lyzhov, A., Molchanov, D., and Vetrov, D. Pitfalls of in-domain uncertainty estimation and ensembling in deep learning. *International Conference on Learning Representations (ICLR)*, 2020.
- Bai, J., Yin, Y., and He, Q. Retinexmamba: Retinex-based mamba for low-light image enhancement. *arXiv preprint arXiv:2405.03349*, 2024.
- Blundell, C., Cornebise, J., Kavukcuoglu, K., and Wierstra, D. Weight uncertainty in neural network. In *International conference on machine learning*, pp. 1613–1622. PMLR, 2015.
- Cai, Y., Bian, H., Lin, J., Wang, H., Timofte, R., and Zhang, Y. Retinexformer: One-stage retinex-based transformer for low-light image enhancement. In *Proceedings of the IEEE/CVF International Conference on Computer Vision*, pp. 12504–12513, 2023.
- Cong, R., Yang, W., Zhang, W., Li, C., Guo, C.-L., Huang, Q., and Kwong, S. Pugan: Physical model-guided underwater image enhancement using gan with dual-discriminators. *IEEE Transactions on Image Processing*, 32:4472–4485, 2023.
- Cong, X., Gui, J., and Hou, J. Underwater organism color fine-tuning via decomposition and guidance. In *Proceedings of the AAAI Conference on Artificial Intelligence*, volume 38, pp. 1389–1398, 2024.
- Dusenberry, M., Jerfel, G., Wen, Y., Ma, Y., Snoek, J., Heller, K., Lakshminarayanan, B., and Tran, D. Efficient and scalable bayesian neural nets with rank-1 factors. In *International conference on machine learning*, pp. 2782–2792. PMLR, 2020.
- Fabbri, C., Islam, M. J., and Sattar, J. Enhancing underwater imagery using generative adversarial networks. In *2018 IEEE international conference on robotics and automation (ICRA)*, pp. 7159–7165. IEEE, 2018.
- Feng, Y., Zhang, C., Wang, P., Wu, P., Yan, Q., and Zhang, Y. You only need one color space: An efficient network for low-light image enhancement. *arXiv preprint arXiv:2402.05809*, 2024.
- Fu, H., Zheng, W., Meng, X., Wang, X., Wang, C., and Ma, H. You do not need additional priors or regularizers in retinex-based low-light image enhancement. In *Proceedings of the IEEE/CVF Conference on Computer Vision and Pattern Recognition*, pp. 18125–18134, 2023a.
- Fu, Z., Wang, W., Huang, Y., Ding, X., and Ma, K.-K. Uncertainty inspired underwater image enhancement. In *European conference on computer vision*, pp. 465–482. Springer, 2022.
- Fu, Z., Yang, Y., Tu, X., Huang, Y., Ding, X., and Ma, K.-K. Learning a simple low-light image enhancer from paired low-light instances. In *Proceedings of the IEEE/CVF conference on computer vision and pattern recognition*, pp. 22252–22261, 2023b.
- Gal, Y. and Ghahramani, Z. Dropout as a bayesian approximation: Representing model uncertainty in deep learning. In *international conference on machine learning*, pp. 1050–1059. PMLR, 2016.
- Graves, A. Practical variational inference for neural networks. *Advances in neural information processing systems*, 24, 2011.
- Grill, J.-B., Strub, F., Althé, F., Tallec, C., Richemond, P., Buchatskaya, E., Doersch, C., Avila Pires, B., Guo, Z., Gheshlaghi Azar, M., et al. Bootstrap your own latent—a new approach to self-supervised learning. *Advances in neural information processing systems*, 33:21271–21284, 2020.
- Gu, A. and Dao, T. Mamba: Linear-time sequence modeling with selective state spaces. *arXiv preprint arXiv:2312.00752*, 2023.
- Guo, C., Li, C., Guo, J., Loy, C. C., Hou, J., Kwong, S., and Cong, R. Zero-reference deep curve estimation for low-light image enhancement. In *Proceedings of the IEEE/CVF conference on computer vision and pattern recognition*, pp. 1780–1789, 2020.
- Guo, X., Li, Y., and Ling, H. Lime: Low-light image enhancement via illumination map estimation. *IEEE Transactions on image processing*, 26(2):982–993, 2016.

- Hai, J., Xuan, Z., Yang, R., Hao, Y., Zou, F., Lin, F., and Han, S. R2rnet: Low-light image enhancement via real-low to real-normal network. *Journal of Visual Communication and Image Representation*, 90:103712, 2023.
- Harrison, J., Willes, J., and Snoek, J. Variational bayesian last layers. In *International Conference on Learning Representations (ICLR)*, 2024.
- He, K., Fan, H., Wu, Y., Xie, S., and Girshick, R. Momentum contrast for unsupervised visual representation learning. In *Proceedings of the IEEE/CVF conference on computer vision and pattern recognition*, pp. 9729–9738, 2020.
- He, K., Chen, X., Xie, S., Li, Y., Dollár, P., and Girshick, R. Masked autoencoders are scalable vision learners. In *Proceedings of the IEEE/CVF conference on computer vision and pattern recognition*, pp. 16000–16009, 2022.
- Hinton, G. E. and Van Camp, D. Keeping the neural networks simple by minimizing the description length of the weights. In *Proceedings of the sixth annual conference on Computational learning theory*, pp. 5–13, 1993.
- Hou, J., Zhu, Z., Hou, J., Liu, H., Zeng, H., and Yuan, H. Global structure-aware diffusion process for low-light image enhancement. *Advances in Neural Information Processing Systems*, 36, 2024.
- Huang, G., Fu, H., and Bors, A. G. Masked image residual learning for scaling deeper vision transformers. *Advances in Neural Information Processing Systems*, 36:57570–57582, 2023a.
- Huang, S., Wang, K., Liu, H., Chen, J., and Li, Y. Contrastive semi-supervised learning for underwater image restoration via reliable bank. In *Proceedings of the IEEE/CVF conference on computer vision and pattern recognition*, pp. 18145–18155, 2023b.
- Huo, F., Li, B., and Zhu, X. Efficient wavelet boost learning-based multi-stage progressive refinement network for underwater image enhancement. In *Proceedings of the IEEE/CVF international conference on computer vision*, pp. 1944–1952, 2021.
- Islam, M. J., Xia, Y., and Sattar, J. Fast underwater image enhancement for improved visual perception. *IEEE Robotics and Automation Letters*, 5(2):3227–3234, 2020.
- Jiang, J., Ye, T., Bai, J., Chen, S., Chai, W., Jun, S., Liu, Y., and Chen, E. Five a⁺ network: You only need 9k parameters for underwater image enhancement. *British Machine Vision Conference (BMVC)*, 2023.
- Jiang, Y., Gong, X., Liu, D., Cheng, Y., Fang, C., Shen, X., Yang, J., Zhou, P., and Wang, Z. Enlightengan: Deep light enhancement without paired supervision. *IEEE transactions on image processing*, 30:2340–2349, 2021.
- Kendall, A. and Cipolla, R. Modelling uncertainty in deep learning for camera relocalization. In *2016 IEEE international conference on Robotics and Automation (ICRA)*, pp. 4762–4769. IEEE, 2016.
- Kendall, A., Badrinarayanan, V., and Cipolla, R. Bayesian segnet: Model uncertainty in deep convolutional encoder-decoder architectures for scene understanding. *arXiv preprint arXiv:1511.02680*, 2015.
- Kendall, A., Gal, Y., and Cipolla, R. Multi-task learning using uncertainty to weigh losses for scene geometry and semantics. In *Proceedings of the IEEE conference on computer vision and pattern recognition*, pp. 7482–7491, 2018.
- Kingma, D. P. Auto-encoding variational bayes. *International Conference on Learning Representations (ICLR)*, 2014. URL <http://arxiv.org/abs/1312.6114>.
- Krishnan, R., Subedar, M., and Tickoo, O. Specifying weight priors in bayesian deep neural networks with empirical bayes. In *Proceedings of the AAAI conference on artificial intelligence*, volume 34, pp. 4477–4484, 2020.
- Lakshminarayanan, B., Pritzel, A., and Blundell, C. Simple and scalable predictive uncertainty estimation using deep ensembles. *Advances in neural information processing systems*, 30, 2017.
- Lee, C., Lee, C., and Kim, C.-S. Contrast enhancement based on layered difference representation of 2d histograms. *IEEE transactions on image processing*, 22(12):5372–5384, 2013.
- Li, C., Guo, C., Ren, W., Cong, R., Hou, J., Kwong, S., and Tao, D. An underwater image enhancement benchmark dataset and beyond. *IEEE transactions on image processing*, 29:4376–4389, 2019a.
- Li, C., Anwar, S., Hou, J., Cong, R., Guo, C., and Ren, W. Underwater image enhancement via medium transmission-guided multi-color space embedding. *IEEE Transactions on Image Processing*, 30:4985–5000, 2021.
- Li, H., Li, J., and Wang, W. A fusion adversarial underwater image enhancement network with a public test dataset. *arXiv preprint arXiv:1906.06819*, 2019b.
- Li, K., Wu, L., Qi, Q., Liu, W., Gao, X., Zhou, L., and Song, D. Beyond single reference for training: Underwater image enhancement via comparative learning. *IEEE Transactions on Circuits and Systems for Video Technology*, 33(6):2561–2576, 2023.

- Liu, R., Fan, X., Zhu, M., Hou, M., and Luo, Z. Real-world underwater enhancement: Challenges, benchmarks, and solutions under natural light. *IEEE transactions on circuits and systems for video technology*, 30(12):4861–4875, 2020.
- Liu, R., Ma, L., Zhang, J., Fan, X., and Luo, Z. Retinex-inspired unrolling with cooperative prior architecture search for low-light image enhancement. In *Proceedings of the IEEE/CVF conference on computer vision and pattern recognition*, pp. 10561–10570, 2021.
- Liu, S., Li, K., and Ding, Y. Underwater image enhancement by diffusion model with customized clip-classifier. *arXiv preprint arXiv:2405.16214*, 2024a.
- Liu, Y. et al. Vmamba: Visual state space model. *arXiv preprint arXiv:2401.10166*, 2024b.
- Ma, K., Zeng, K., and Wang, Z. Perceptual quality assessment for multi-exposure image fusion. *IEEE Transactions on Image Processing*, 24(11):3345–3356, 2015.
- Mittal, A., Soundararajan, R., and Bovik, A. C. Making a “completely blind” image quality analyzer. *IEEE Signal processing letters*, 20(3):209–212, 2012.
- Neal, R. M. *Bayesian learning for neural networks*, volume 118. Springer Science & Business Media, 2012.
- Panetta, K., Gao, C., and Agaian, S. Human-visual-system-inspired underwater image quality measures. *IEEE Journal of Oceanic Engineering*, 41(3):541–551, 2015.
- Pang, T., Quan, Y., and Ji, H. Self-supervised bayesian deep learning for image recovery with applications to compressive sensing. In *Computer Vision—ECCV 2020: 16th European Conference, Glasgow, UK, August 23–28, 2020, Proceedings, Part XI 16*, pp. 475–491. Springer, 2020.
- Peng, L., Zhu, C., and Bian, L. U-shape transformer for underwater image enhancement. *IEEE Transactions on Image Processing*, 2023.
- Radford, A., Kim, J. W., Hallacy, C., Ramesh, A., Goh, G., Agarwal, S., Sastry, G., Askell, A., Mishkin, P., Clark, J., et al. Learning transferable visual models from natural language supervision. In *International conference on machine learning*, pp. 8748–8763. PMLR, 2021.
- Reza, A. M. Realization of the contrast limited adaptive histogram equalization (clahe) for real-time image enhancement. *Journal of VLSI signal processing systems for signal, image and video technology*, 38:35–44, 2004.
- Robbins, H. An empirical bayes approach to statistics. *Proceedings of the Third Berkeley Symposium on Mathematical Statistics and Probability*, 1:157–163, 1956.
- Shi, W., Caballero, J., Huszár, F., Totz, J., Aitken, A. P., Bishop, R., Rueckert, D., and Wang, Z. Real-time single image and video super-resolution using an efficient sub-pixel convolutional neural network. In *Proceedings of the IEEE conference on computer vision and pattern recognition*, pp. 1874–1883, 2016.
- Tang, Y., Kawasaki, H., and Iwaguchi, T. Underwater image enhancement by transformer-based diffusion model with non-uniform sampling for skip strategy. In *Proceedings of the 31st ACM International Conference on Multimedia*, pp. 5419–5427, 2023.
- Tomczak, M., Swaroop, S., Foong, A., and Turner, R. Collapsed variational bounds for bayesian neural networks. *Advances in Neural Information Processing Systems*, 34: 25412–25426, 2021.
- Ulyanov, D. Instance normalization: The missing ingredient for fast stylization. *arXiv preprint arXiv:1607.08022*, 2016.
- Vaswani, A., Shazeer, N., Parmar, N., Uszkoreit, J., Jones, L., Gomez, A. N., Kaiser, Ł., and Polosukhin, I. Attention is all you need. *Advances in neural information processing systems*, 30, 2017.
- Vonikakis, V., Kouskouridas, R., and Gasteratos, A. On the evaluation of illumination compensation algorithms. *Multimedia Tools and Applications*, 77:9211–9231, 2018.
- Wang, J., Chan, K. C., and Loy, C. C. Exploring clip for assessing the look and feel of images. In *Proceedings of the AAAI Conference on Artificial Intelligence*, volume 37, pp. 2555–2563, 2023.
- Wang, S., Zheng, J., Hu, H.-M., and Li, B. Naturalness preserved enhancement algorithm for non-uniform illumination images. *IEEE transactions on image processing*, 22(9):3538–3548, 2013.
- Wang, Y., Wan, R., Yang, W., Li, H., Chau, L.-P., and Kot, A. Low-light image enhancement with normalizing flow. In *Proceedings of the AAAI conference on artificial intelligence*, volume 36, pp. 2604–2612, 2022.
- Wei, C., Wang, W., Yang, W., and Liu, J. Deep retinex decomposition for low-light enhancement. *British Machine Vision Conference (BMVC)*, 2018.
- Wilson, A. G. and Izmailov, P. Bayesian deep learning and a probabilistic perspective of generalization. *Advances in neural information processing systems*, 33:4697–4708, 2020.
- Xu, K., Yang, X., Yin, B., and Lau, R. W. Learning to restore low-light images via decomposition-and-enhancement. In *Proceedings of the IEEE/CVF conference on computer vision and pattern recognition*, pp. 2281–2290, 2020.

- Xu, X., Wang, R., Fu, C.-W., and Jia, J. Snr-aware low-light image enhancement. In *Proceedings of the IEEE/CVF conference on computer vision and pattern recognition*, pp. 17714–17724, 2022.
- Yang, M. and Sowmya, A. An underwater color image quality evaluation metric. *IEEE Transactions on Image Processing*, 24(12):6062–6071, 2015.
- Yang, W., Wang, W., Huang, H., Wang, S., and Liu, J. Sparse gradient regularized deep retinex network for robust low-light image enhancement. *IEEE Transactions on Image Processing*, 30:2072–2086, 2021.
- Zamir, S. W., Arora, A., Khan, S., Hayat, M., Khan, F. S., and Yang, M.-H. Restormer: Efficient transformer for high-resolution image restoration. In *Proceedings of the IEEE/CVF Conference on Computer Vision and Pattern Recognition (CVPR)*, pp. 5728–5739, 2022.
- Zhang, W., Zhuang, P., Sun, H.-H., Li, G., Kwong, S., and Li, C. Underwater image enhancement via minimal color loss and locally adaptive contrast enhancement. *IEEE Transactions on Image Processing*, 31:3997–4010, 2022.
- Zhang, Y., Zhang, J., and Guo, X. Kindling the darkness: A practical low-light image enhancer. In *Proceedings of the 27th ACM international conference on multimedia*, pp. 1632–1640, 2019.
- Zhao, C., Cai, W., Dong, C., and Hu, C. Wavelet-based fourier information interaction with frequency diffusion adjustment for underwater image restoration. In *Proceedings of the IEEE/CVF Conference on Computer Vision and Pattern Recognition*, pp. 8281–8291, 2024.
- Zhou, H., Dong, W., Liu, X., Liu, S., Min, X., Zhai, G., and Chen, J. Glare: Low light image enhancement via generative latent feature based codebook retrieval. *Proceedings of the European conference on computer vision (ECCV)*, 2024.
- Zhu, J.-Y., Park, T., Isola, P., and Efros, A. A. Unpaired image-to-image translation using cycle-consistent adversarial networks. In *Proceedings of the IEEE international conference on computer vision*, pp. 2223–2232, 2017.

A. Mamba and Transformer Backbones

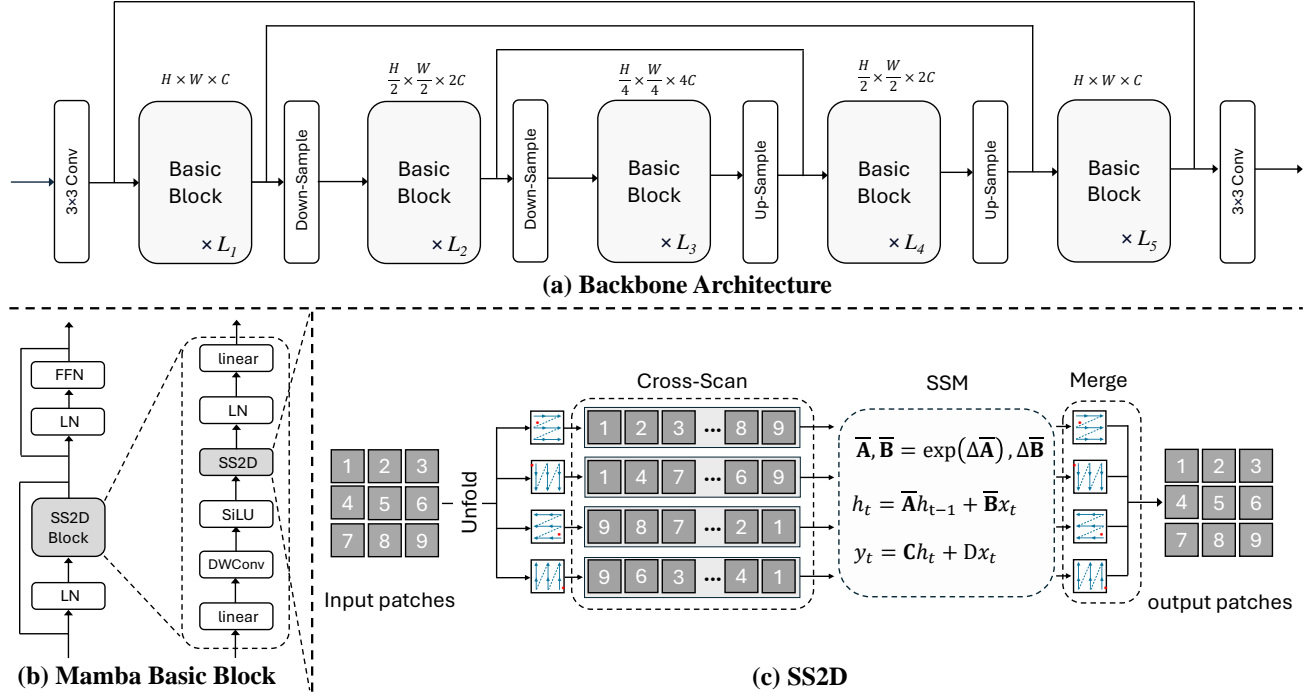


Figure 9: Overview of the backbone architecture, consisting of five feature stages, each comprising L_i basic blocks. The shortcut connections are implemented using addition. Panel (a) illustrates the hierarchical structure of the backbone. Panel (b) details the basic Block, including its integration with the SS2D module. Panel (c) explains the SS2D mechanism, incorporating Cross-Scan, structured state-space modelling (SSM), and patch merging. Further details about SS2D can be found in (Liu et al., 2024b). For the Transformer backbone, we simply replace the basic block with Transformer block in (Zamir et al., 2022).

We consider using both Mamba and Transformer as the backbone architecture of our BEM. As shown in Figure 9, the overall framework is akin to a U-Net, which consists of an input convolutional layer, $L_1 + L_2 + L_3 + L_4 + L_5$ basic blocks, and an output convolutional layer. After each downsampling operation, the spatial dimensions of the feature maps are halved, while the number of channels is doubled. Specifically, given an input image with a shape of $H \times W \times 3$, the encoding blocks obtain hierarchical feature maps of sizes $H \times W \times C$, $\frac{H}{2} \times \frac{W}{2} \times 2C$ and $\frac{H}{4} \times \frac{W}{4} \times 4C$. In the last two feature stages, the features are upsampled with the `pixelshuffle` layers (Shi et al., 2016). At each scale level, lateral connections are built to link the corresponding blocks in the encoder and decoder.

Construct the Transformer backbone. Given the availability of a mature Transformer architecture for image restoration (Zamir et al., 2022), we reuse their Transformer block, which features transposed attention, as the basic block of our Transformer backbone.

Construct the Mamba backbone. For the Mamba backbone, we adopt the basic block design in VMamba (Liu et al., 2024b) to build the U-Net Mamba backbone, where each basic block is composed of a 2D Selective Scan (SS2D) module (Liu et al., 2024b) and a feedforward network (FFN). The formulation of the Mamba block (Liu et al., 2024b) in layer l can be expressed as

$$\begin{aligned} \mathbf{h}_l &= \text{SS2D}(\text{LN}(\mathbf{h}_{l-1})) + \mathbf{h}_{l-1}, \\ \mathbf{h}_{l+1} &= \text{FFN}(\text{LN}(\mathbf{h}_l)) + \mathbf{h}_l, \end{aligned} \quad (12)$$

where FFN denotes the feedforward network and LN denotes layer normalisation. \mathbf{h}_{l-1} and \mathbf{h}_l denote the input and output in the l -th layer, respectively.

We build our backbone by gradually evaluating each configuration of a vanilla Mamba-based UNet. We thoroughly

investigate settings including `ssm-ratio`, block numbers, `n_feat` and `mlp-ratio`. The training strategies for all variants are identical. Setting `n_feat` denotes the number of feature maps in the first `conv3×3`'s output. Setting `d_state` denotes the state dimension of SSM. Note that the established baseline assures two things: 1) Further naively introducing additional parameters and FLOPs, e.g., scaling models with more blocks, will not help boost the performance. 2) A technique with additional parameters introduced to the baseline model can no doubt demonstrate its effectiveness if the modified model shows better results than the baseline.

Table 4: The performance of deterministic Mamba UNet variants with different `d_state`, `ssm-ratio`, `mlp-ratio`, `n_feat` and block numbers. PSNR and SSIM on LOL-v1 are reported. Since the deterministic networks trained using minibatch optimisation are likely to fit very different targets each time, the results will fluctuate greatly. We train each model five times and report the average performance.

| <code>d_state</code> | <code>ssm-ratio</code> | <code>mlp-ratio</code> | <code>n_feat</code> | block numbers | FLOPs (G) | Params (M) | TP (img/s) | PSNR (dB) | SSIM |
|----------------------|------------------------|------------------------|---------------------|---------------|-----------|------------|------------|-----------|-------|
| 1 | 1 | 2.66 | 40 | [2,2,2] | 14.25 | 1.23 | 125 | 22.45 | 0.828 |
| 1 | 1 | 4 | 40 | [2,2,2] | 20.41 | 1.52 | 78 | 23.76 | 0.842 |
| 16 | 1 | 2.66 | 40 | [2,2,2] | 25.50 | 1.37 | 84 | 23.83 | 0.840 |
| 32 | 1 | 2.66 | 40 | [2,2,2] | 37.49 | 1.52 | 61 | 21.93 | 0.812 |
| 16 | 2 | 4 | 40 | [2,2,2] | 44.36 | 2.08 | 58 | 23.67 | 0.830 |
| 16 | 2 | 4 | 52 | [2,2,2] | 65.10 | 3.37 | 40 | 23.21 | 0.833 |
| 16 | 2 | 4 | 40 | [2,2,2,2] | 54.82 | 7.77 | 51 | 23.44 | 0.838 |
| 1 | 2 | 4 | 40 | [2,2,2] | 21.87 | 1.79 | 82 | 22.73 | 0.834 |

To balance both speed and performance, we selected the model in the second row of Table 4 as the backbone for our BEM. The chosen backbone features a simple architecture with no task-specific modules, enhancing its generalisability and establishing a solid foundation for extending our method to other types of vision tasks.

B. Momentum prior

BNNs with high-dimensional weight spaces often encounter challenges such as underfitting or even non-convergence, as noted by [Dusenberry et al. \(2020\)](#); [Tomczak et al. \(2021\)](#). This limitation is a significant factor hindering BNN’s performance in low-level vision tasks.

We address this in Sec. 3.2 by introducing the Momentum prior, $P(\mathbf{w}) = \mathcal{N}(\mathbf{w}; \mu_t^{\text{EMA}}, \sigma_t^{\text{EMA}^2} \mathbf{I})$. The motivation for the Momentum prior is as follows: it begins with a naive Gaussian prior early in training, providing useful inductive biases ([Wilson & Izmailov, 2020](#)). However, as training progresses, relying on a fixed, simple prior (e.g., $P(\mathbf{w}) = \mathcal{N}(\mathbf{w}; \mathbf{0}, \mathbf{I})$) can limit the network’s capacity to fit the data effectively. To address this, the Momentum prior gradually updates its parameters with empirical information from the data during training. Another motivation for using the Momentum prior is our observation that during DNN training (e.g., over 150K iterations), the results start oscillating around 80K iterations. These oscillations occasionally produce good results but often revert back, failing to stabilise. The Momentum prior effectively captures and summarises these late-stage oscillations, which can be considered a form of predictive uncertainty, thereby better guiding the updates to the BNN’s posterior parameters.

The Momentum prior is akin to the Momentum teacher ([He et al., 2020](#); [Grill et al., 2020](#)) in self-supervised learning, but the Momentum prior instead regularises the variational posterior parameters rather than the outputs. This simple yet effective approach significantly improves BNN performance in our tasks. Additionally, the Momentum prior also shares similarities with deep learning ensembles ([Lakshminarayanan et al., 2017](#)), a key strategy for uncertainty estimation, as per [Ashukha et al. \(2020\)](#).

Impact of Different Priors. We compare the Momentum prior with the naive Gaussian prior and empirical Bayes prior. The naive Gaussian prior is defined as $P(\mathbf{w}) = \mathcal{N}(\mathbf{w}; \mathbf{0}, 0.1^2 \mathbf{I})$. The empirical Bayes prior, MOPED ([Krishnan et al., 2020](#)), is defined as $P(\mathbf{w}) = \mathcal{N}(\mathbf{w}; \mathbf{w}^{\text{MLE}}, 0.1^2 \mathbf{I})$, where \mathbf{w}^{MLE} represents the maximum likelihood estimate (MLE) of the weights learned by optimising a deterministic network. In the case of the empirical Bayes prior, the mean μ of the variational posterior $q(\mathbf{w}|\theta)$ is initialised as the MLE of the weights, \mathbf{w}^{MLE} , and the posterior variance σ is set to $0.1|\mathbf{w}^{\text{MLE}}|$, as suggested by [Krishnan et al. \(2020\)](#). As shown in Figure 10, the Momentum prior demonstrates a clear advantage over

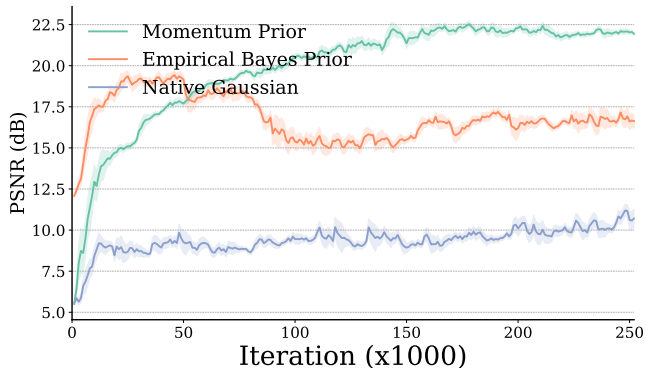


Figure 10: Training curves of one-stage BNNs with different priors. The PSNR for each iteration is calculated using the mean weight μ .

both baselines. Although the empirical Bayes prior accelerates training in the early iterations, its performance deteriorates over time due to its fixed nature. Additionally, we observed that BNNs with the empirical Bayes prior tend to exhibit very large gradients, with the average gradient norm reaching as high as 500 during training. After applying gradient clipping, the parameters of the model with the empirical Bayes prior tend to stagnate after a certain number of iterations, oscillating without significant updates. The naive Gaussian prior, $P(\mathbf{w}) = \mathcal{N}(\mathbf{w}; \mathbf{0}, 0.1^2\mathbf{I})$, essentially acts as weight regularisation for BNNs. This regularisation is overly restrictive, preventing the BNN from fitting a complex distribution. In Table 5, we present the PSNR values on the training and test sets of LOL-v1, both of which are unusually low when using naive Gaussian and empirical priors. These observations lead us to hypothesise that the failure of these models is due to underfitting. Unlike

Table 5: Comparison of various priors on the training and test sets on LOL-v1. A one-stage BNN is used to obtain the reported results.

| | Naive Gaussian Prior | Empirical Bayes Prior | Momentum Prior |
|--------------|----------------------|-----------------------|----------------|
| Training Set | 12.36 | 18.63 | 25.08 |
| Test Set | 11.84 | 18.04 | 22.56 |

empirical Bayes (Robbins, 1956; Krishnan et al., 2020), which defines a static prior based on MLE-optimized parameters, our momentum-based strategy incrementally refines the prior during training. This continuous adaptation prevents the loss function in Equation (5) from being minimized primarily by reducing the prior matching term, $\text{KL}[q(\mathbf{w}|\boldsymbol{\theta})\|P(\mathbf{w})]$, and instead ensures a stronger focus on data-driven learning through the data-dependent term in Equation (5).

C. Analysis of Predictive Uncertainty

In this section, we statistical analyse of the diversity in predictions generated by BEM. Table 6 presents the predictive uncertainty statistics collected from the LOL-v1 dataset. A larger standard deviation indicates higher uncertainty, suggesting that the BEM produces more diverse predictions and better captures the one-to-many mapping nature of the task. The maximum values approximate the upper bound of the BEM’s predictive quality, while the minimum values approximate its lower bound.

As shown in Table 6, the minimum CLIP-IQA values in the LOL dataset are significantly smaller than the maximum values, potentially reflecting the presence of low-quality GT images in the dataset. We hypothesise that these poor-quality GT images significantly impact the performance of deterministic neural networks. However, due to BEM’s uncertainty modelling, such low-quality GT images primarily affect the lower bound of BEM’s predictive quality, minimising their overall influence on performance.

In Figure 11, we randomly selected an input image from the heterogeneous dataset LSRW (Hai et al., 2023) to analyse the distribution of its prediction results. We observe that, for each metric, although many predictions fall within the central range, they are not overly concentrated. This demonstrates the diversity of the model’s predictions.

Table 6: Statistic data on predictive uncertainty on LOL-v1. CLIP (Brightness) indicate the CLIP feature similarity using text prompt “Bright photo”. Likewise, CLIP (Quality) use prompt “Good photo”.

| Metric | Maximum | Mean | Median | Minimum | Standard deviation |
|------------------------------------|---------|--------|--------|---------|--------------------|
| PSNR | 26.89 | 22.87 | 22.97 | 17.90 | 1.911 |
| SSIM | 0.876 | 0.855 | 0.856 | 0.819 | 0.013 |
| CLIP-IQA (Brightness) $\times 100$ | 93.62 | 89.63 | 89.71 | 84.20 | 1.689 |
| CLIP-IQA (Quality) $\times 100$ | 64.34 | 59.13 | 59.08 | 54.22 | 1.825 |
| CLIP-IQA (Noisiness) $\times 100$ | 36.17 | 30.06 | 30.02 | 25.08 | 1.942 |
| Negative NIQE | -4.647 | -4.808 | -4.806 | -4.971 | 0.059 |

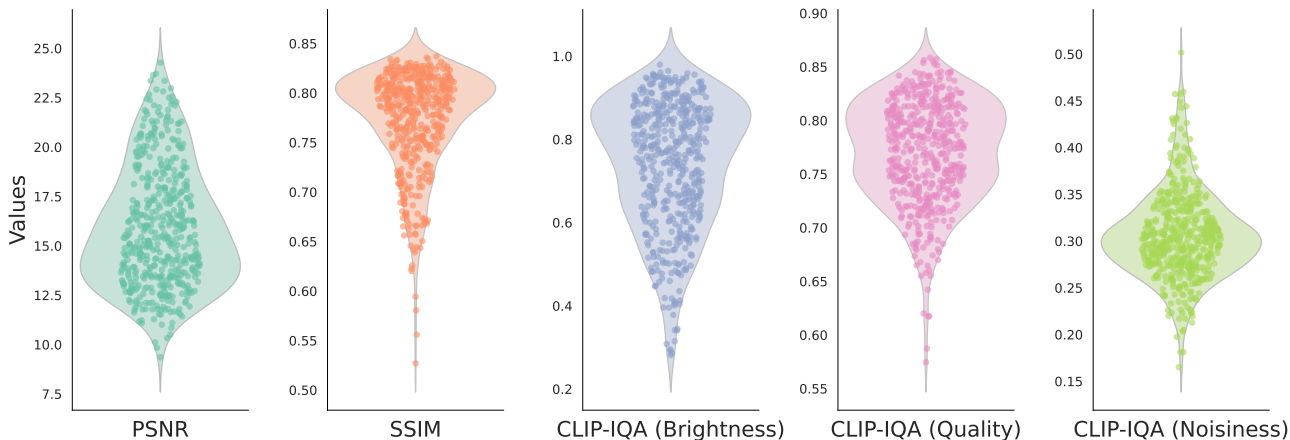
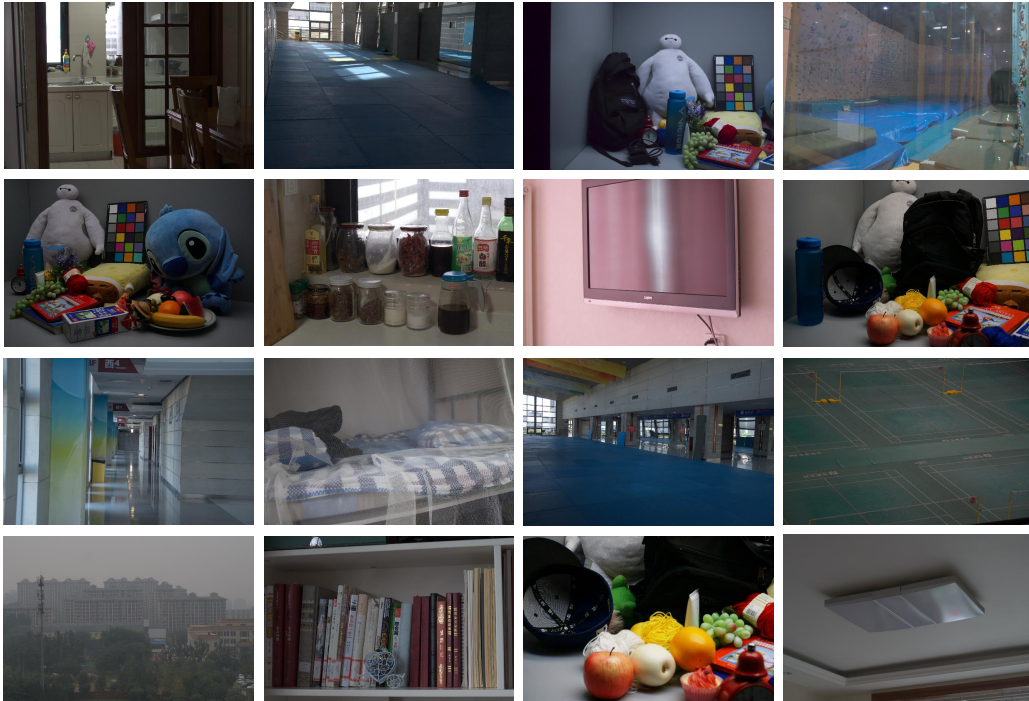


Figure 11: Distribution of 500 random predictions generated by the BEM model for a single low-light image across different evaluation metrics, including PSNR, SSIM, and three CLIP-IQA metrics (“Brightness”, “Quality”, “Noisiness”). Each violin plot visualises the density and range of predictions.

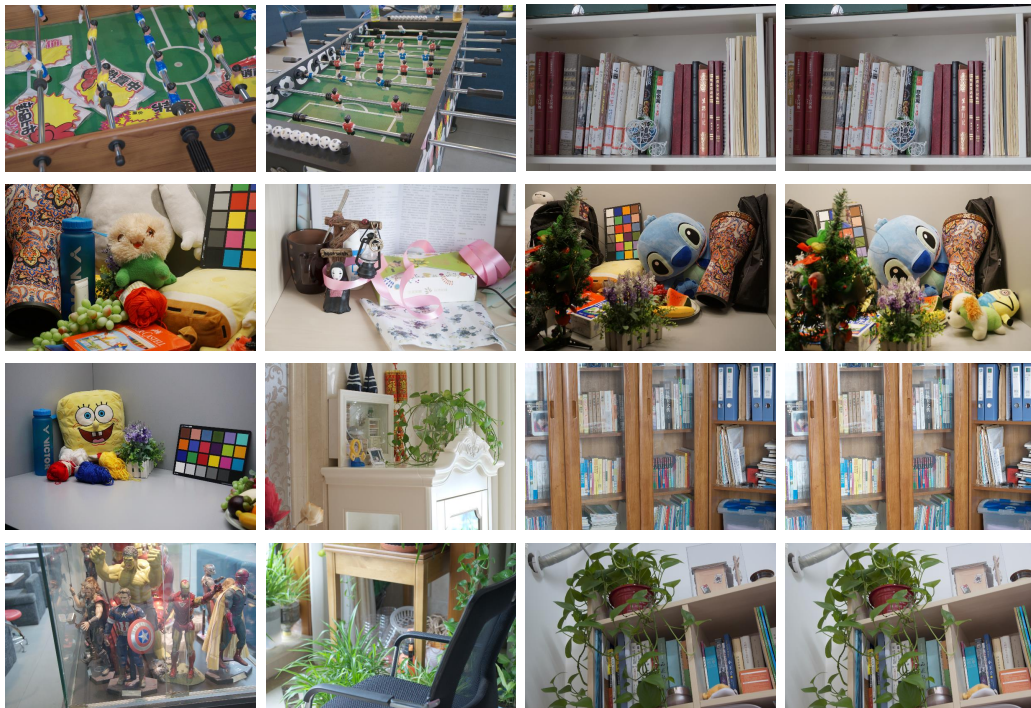
To investigate how the predictive uncertainty and quality of BEM are influenced by the overall GT quality in the training data, we conduct the following experiments as detailed in Appendices C.1 and C.2.

C.1. Step one: Identify low-quality GT images in Training Data

To separate training data with low-quality GT images from the dataset, we initially employed CLIP-IQA (Wang et al., 2023) with text prompts (“Brightness”, “Noisiness”, “Quality”) to filter out images with low brightness, high noise levels, and poor quality. This automated process was followed by manual refinement to identify and separate poor-quality GT images. Examples of low-quality GT images from the LOL and UIEB training sets are shown in Figure 12 and Figure 13, alongside high-quality GT images for comparison. While the algorithmic filtering reduced excessive subjectivity, the manual refinement process may still introduce some subjective bias. Therefore, the separation results should be treated as indicative rather than definitive.

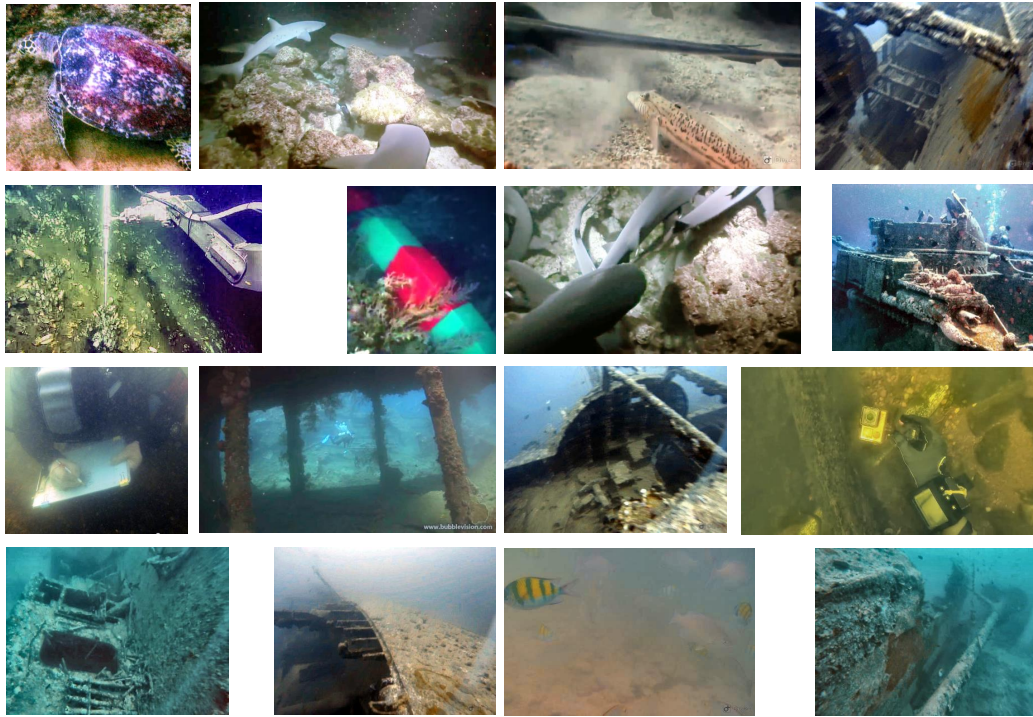


Low-Quality GT Images

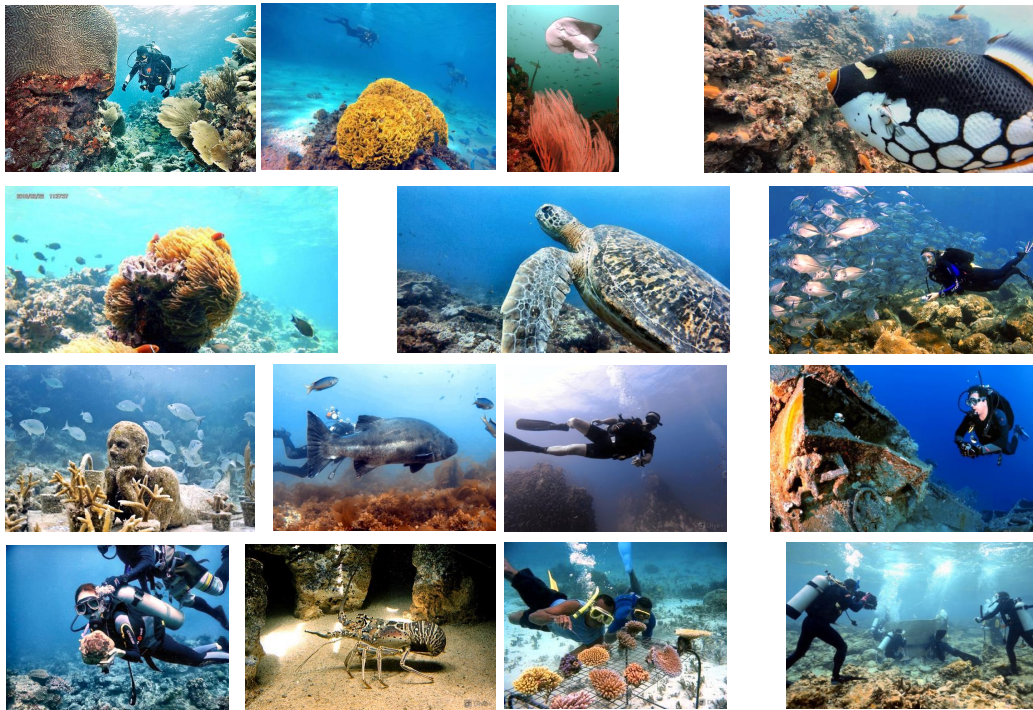


High-Quality GT Images

Figure 12: Examples of low-quality and high-quality GT images from the LOL training set. The categorisation may be influenced by subjective biases in assessing visual clarity, lighting, and overall image quality.



Low-Quality GT Images



High-Quality GT Images

Figure 13: Examples of low-quality and high-quality GT images from the UIEB training set. The categorisation may be influenced by subjective biases in assessing visual clarity, lighting, and overall image quality.

C.2. STEP Two: Impact of Training Data Quality on Predictive Performance

When the dataset contains low-quality ground-truth images, BEM generates a distribution of predictive quality, producing both high-quality and low-quality outputs. The probability of generating high-quality outputs is influenced by the proportion of high-quality ground-truth images in the training data.

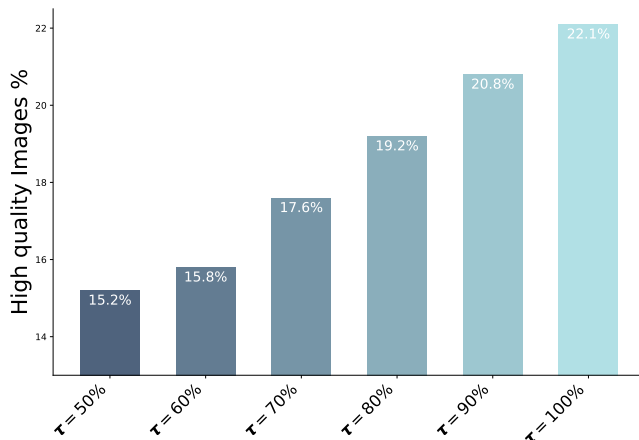


Figure 14: Impact of training data quality on BEM. The x-axis represents the proportion of high-quality images in the training dataset (τ), while the y-axis shows the percentage of high-quality predictions obtained after $K = 100$ sampling times on the test set. Higher proportions of high-quality training data lead to a greater likelihood of generating high-quality predictions. A prediction is classified as high-quality if its CLIP (Quality) score exceeds 0.8.

Specifically, as the proportion of high-quality ground-truth images increases, the probability of sampling high-quality outputs during inference also rises. Consequently, fewer sampling iterations are required to obtain satisfactory enhancement results. Conversely, when the proportion of high-quality ground-truth images is low, more sampling iterations are needed.

To examine whether the proportion of high-quality ground-truth (GT) images in the training data affects the likelihood of generating high-quality outputs, we pose the question: Does increasing the share of high-quality images in the training set improve the probability of producing high-quality results?

To test this hypothesis, we conducted the following experiment: First, using the sample separation method described in Sec. C.1, we identified and labelled low-quality GT images in the training dataset. Next, while keeping the total size of the training dataset constant, we systematically replaced low-quality GT images in the LOL-v1 training set with high-quality GT images from the LOL-v2-real dataset. This allowed us to control the proportion of high-quality images in the training data, denoted as τ .

The results, shown in Figure 14, demonstrate a clear trend: as the proportion of low-quality GT images decreases, the likelihood of generating high-quality outputs increases consistently. When the training dataset consists entirely of high-quality GT images ($\tau = 100\%$), BEM achieves significant efficiency, producing a satisfactory enhanced output approximately once every five sampling iterations on average. This highlights the direct relationship between training data quality and the predictive performance of BEM. Nonetheless, the true strength of BEM lies in its ability to generate high-quality enhanced images even when real-world data contains low-quality GT images, thanks to its uncertainty modelling capabilities. The trade-off, however, is the need for more sampling attempts.

C.3. Enhanced Images Beyond the Ground Truth

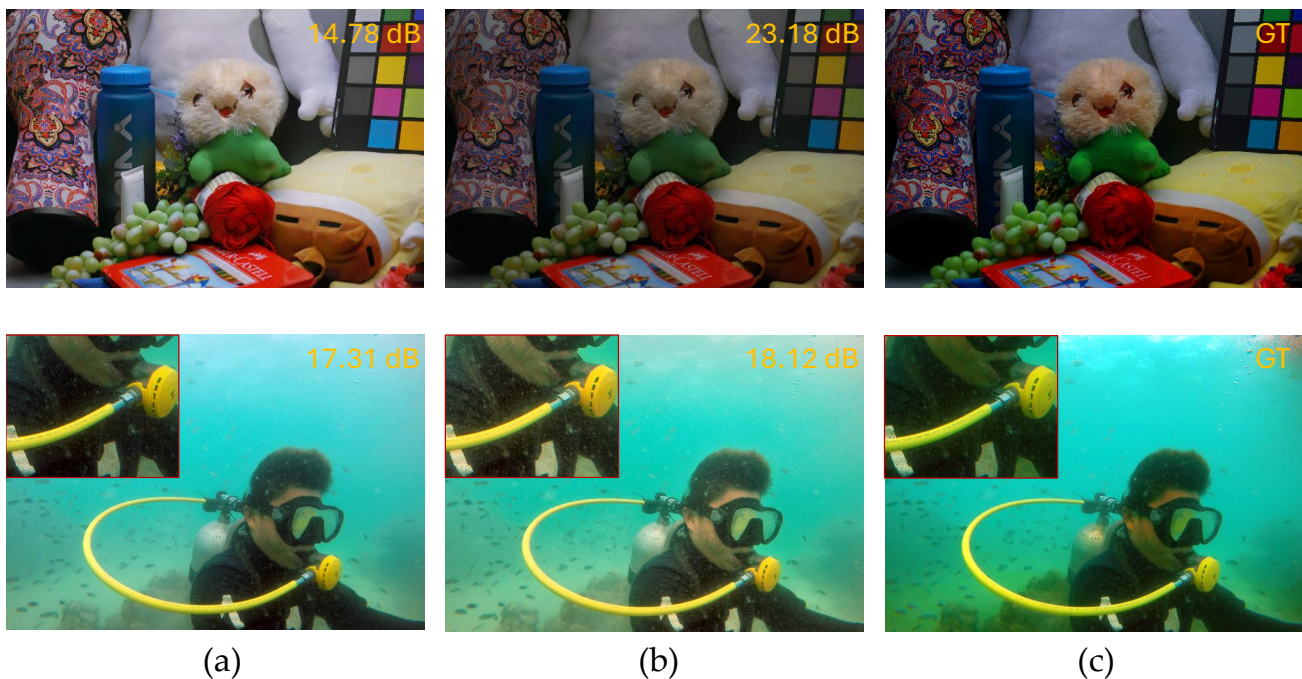


Figure 15: A superior enhancement does not necessarily align with the suboptimal ground truth. The left and middle images represent two plausible outputs from BEM, showcasing diverse enhancements. The left images are selected using the no-reference CLIP-IQA (Qualify) metric, while the middle images are chosen based on the full-reference PSNR metric.

As illustrated in Figure 15, the ground-truth images in the test set are low-quality. When evaluated using full-reference metrics such as MSE or PSNR, BEM produces outputs like image (b), which closely resemble the low-quality GT image. In contrast, when using CLIP-IQA as a no-reference metric, BEM generates outputs like image (a). Upon observation, image (a) demonstrates superior illumination and clarity compared to image (b) in Figure 15.

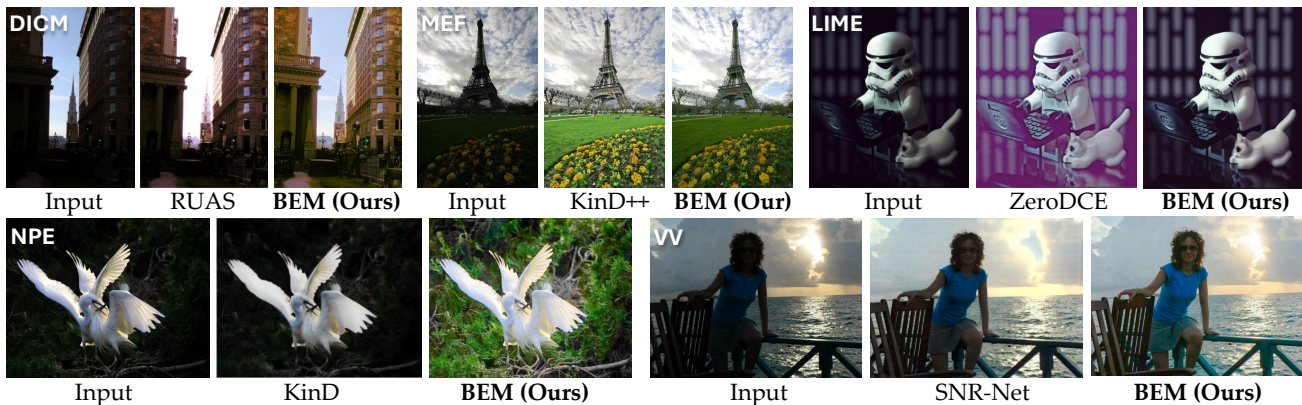


Figure 16: Visual comparisons on the DICM, LIME, MEF, NPE and VV datasets.

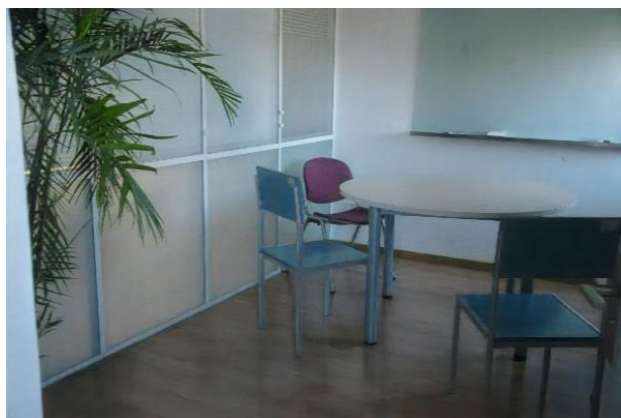
D. Supplementary Visualisations

More visualisation for LLIE. Visual comparisons on five unpaired LLIE test sets are shown in Figure 16, where our restored images offer better perceptual improvement. For example, in DICM, our method enhances brightness while effectively avoiding overexposure.

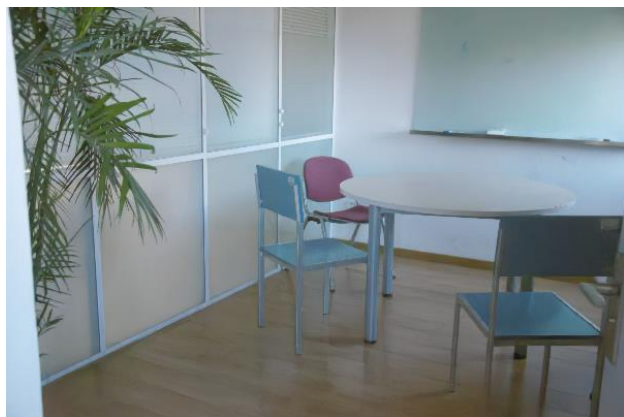
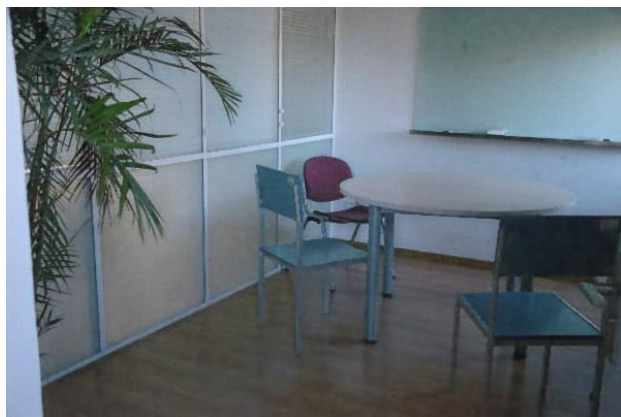
To facilitate a closer inspection of enhanced image details, we present high-resolution visual comparisons in Figure 17, where the predictions of state-of-the-art models are displayed at their original resolutions. The high-resolution visualisation reveals that previous state-of-the-art methods tend to exhibit varying degrees of noise artefacts in the enhanced results, significantly degrading perceptual quality. In contrast, our method effectively suppresses these noise artefacts, which are often introduced by low-light conditions. Furthermore, our approach achieves superior detail restoration, while other methods show signs of blurring and detail loss.



KinD



SNR-Net

**BEM (Ours)**

RetinexFormer

Figure 17: Visual comparisons with KinD, SNR-Net and RetinexFormer under images' original resolution. The sample is from the LOL-v2-real dataset.

More Visualisations for UIE. In Figure 18, we visually compare our BEM with other UIE methods, including WaterNet (Li et al., 2019a), PRWNet (Huo et al., 2021), FUnIEGAN (Islam et al., 2020), PUGAN (Cong et al., 2023), MMLE (Zhang et al., 2022), PUIE-MP (Fu et al., 2022), FiveA+(Jiang et al., 2023), CLUIE (Li et al., 2023), Semi-UIR (Huang et al., 2023b), UColor (Li et al., 2021), DM-Underwater (Tang et al., 2023), and CLIP-UIE (Liu et al., 2024a). In deeper ocean images with dominant blueish effects (last row, BEM can better enhance visual clarity on the UIEB-R90, C60 and U45 datasets. In Figure 19, we present additional visual comparisons on the U45 and UCCS datasets, demonstrating that our method consistently outperforms PUGAN and PUIE-MP in enhancing various underwater scenes.

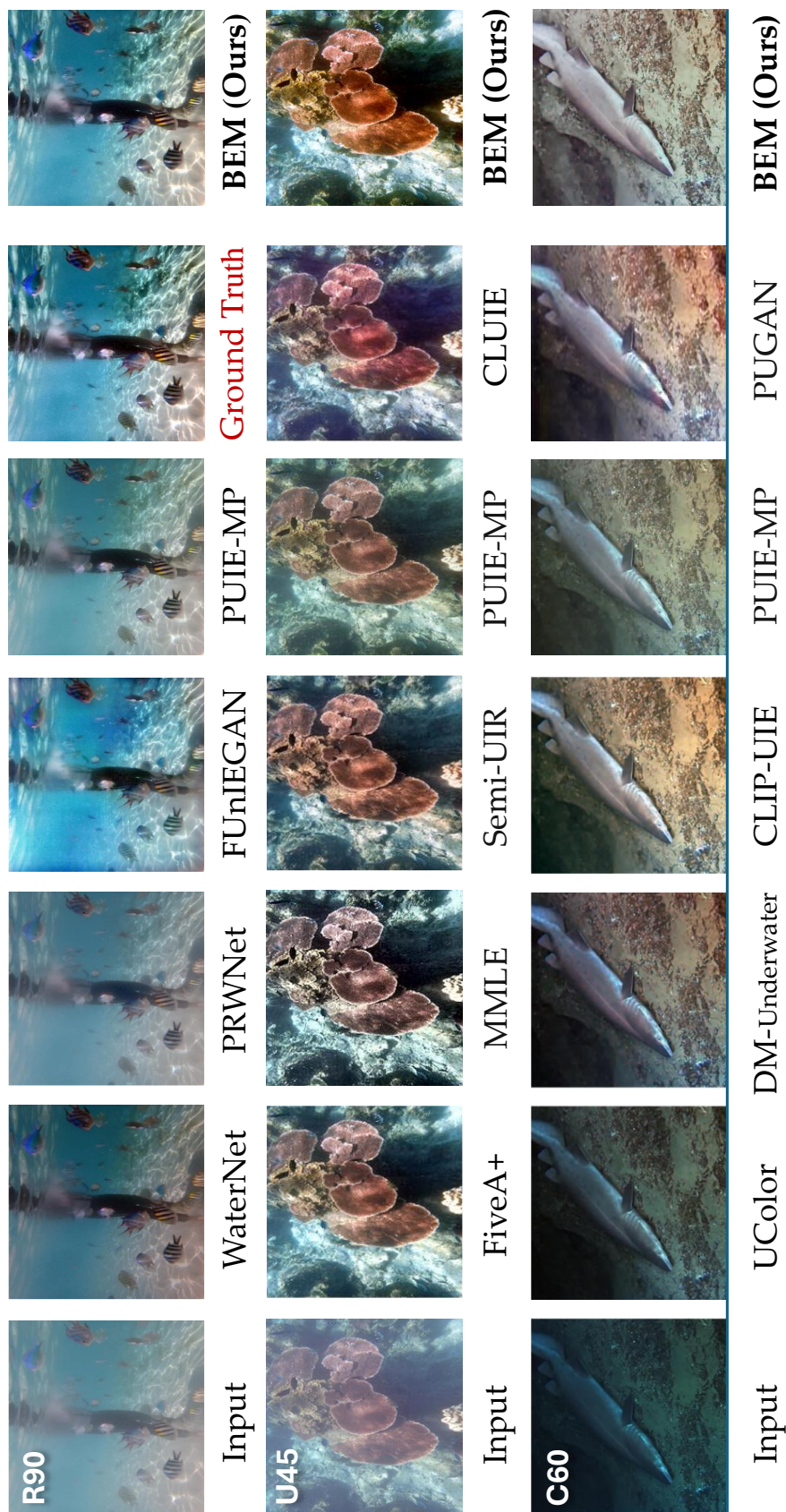
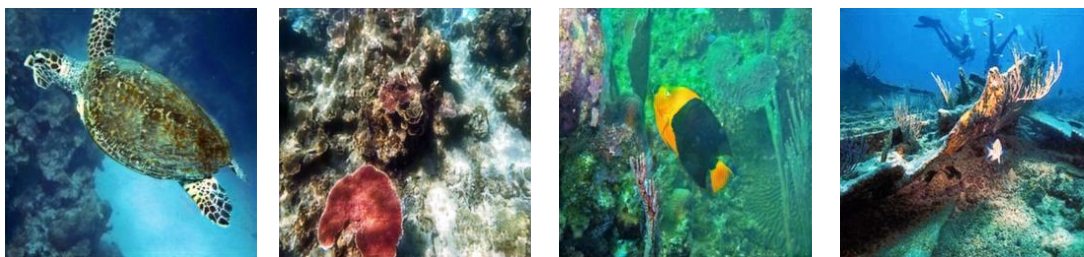
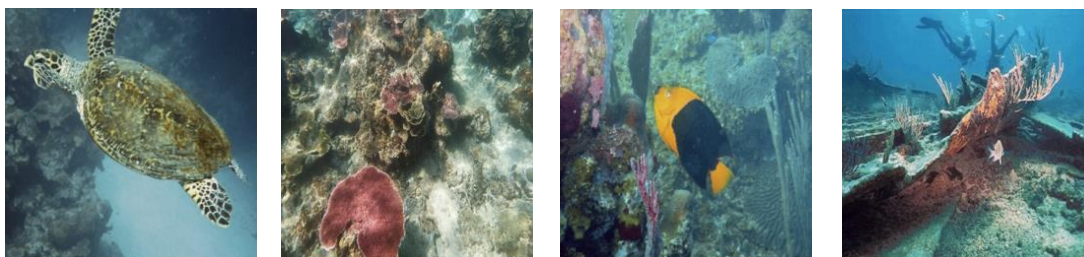


Figure 18: Detailed visual comparisons of our BEM with twelve SOTA UIE methods.

PUGAN



PUIE-MP



**BEM
(Ours)**



U45

PUGAN



PUIE-MP



**BEM
(Ours)**



UCCS

Figure 19: Visual comparisons with PUGAN and PUIE-MP on the U45 and UCCS test sets.

E. Controllable Local Enhancement

Thanks to the interpretability of the lower-dimensional representations in both the spatial and channel dimensions, we can easily achieve local adjustment with a masking strategy. The local adjustment is particularly useful in the cases where the input images are unevenly distorted, and we want to retain the undistorted regions consistent before and after enhancement. The local adjustment process can be achieved by using a mask layer \mathbf{M} : $\mathbf{y}^{\text{local}} = G(\gamma\mathbf{M} \odot \mathbf{v}, \mathbf{x}; \mathbf{w}^G)$, where \mathbf{v} can be lower-dimensional features extracted from a real image or estimated by the first stage model via Equation (9). We can use a scalar γ to control the strength of the enhancement effect. A demonstration of the local enhancement is shown in Figure 20.

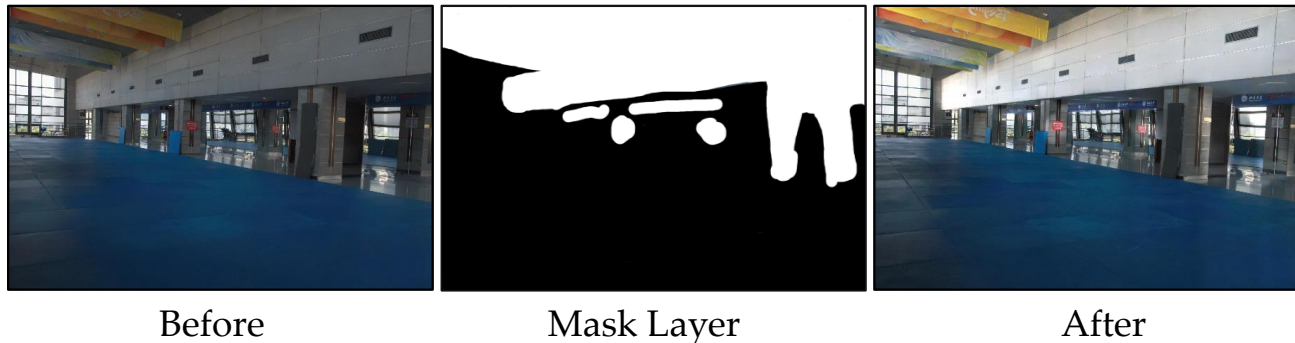


Figure 20: The local brightness of an image before adjustment (left) can be edited locally by providing a mask layer (middle). The image after adjustment (right) shows improved brightness in the regions indicated by the mask.

Compared to directly applying the mask to the output, our local enhancement strategy not only reduces the dependency on mask accuracy but also results in smoother transitions at the mask boundaries. This mitigates issues such as excessive roughness or colour inconsistencies between processed and unprocessed regions.

F. Label Diversity Augmentation

Theoretically, an infinite number of target images could correspond to a single input. However, current paired datasets often lack sufficient label diversity, which may become a bottleneck for BEM model performance.

Table 7: Evaluation of label augmentation strategies for enhancing label diversity. PSNR scores are obtained using single-stage models on LOL-v1.

| Model | Gamma Correction | Saturation Shift | CLAHE | PSNR \uparrow |
|-------|------------------|------------------|-------|-----------------|
| BEM | | | | 24.78 |
| BEM | ✓ | | | 24.89 |
| BEM | ✓ | ✓ | | 24.93 |
| BEM | ✓ | ✓ | ✓ | 24.86 |
| DNN | | | | 24.02 |
| DNN | ✓ | ✓ | ✓ | 21.58 |

Without relying on additional data collection to increase label diversity, we propose two strategies for augmenting label diversity within existing datasets:

- i) When training a deep network, high-resolution images are often divided into smaller crops (e.g., 128×128). Many of these smaller image crops may represent the same scene, but due to various factors, such as being captured at different moments in a video or having different capture settings, the corresponding target crops show differences in colour or brightness. Thus, using these crops as input during training, the actual label diversity within the training data is naturally increased.
- ii) Existing labels can be further enriched by applying data augmentation techniques such as random brightness adjustments, saturation shifts, changes in colour temperature, gamma corrections, and histogram equalisation.

Both strategies contribute to increasing label diversity to some extent.

In Table 7, we evaluate whether expanding the number of target images using gamma correction, saturation shift, and CLAHE (Reza, 2004) can further improve the model’s performance. Among these, saturation shift is a linear transformation, while gamma correction and CLAHE are nonlinear methods. We observed that deterministic networks showed a decline in performance after applying these label augmentation techniques. This can be attributed to DNNs overfitting to local solutions that deviate further from the inference image as uncertainty in the data increases. In contrast, BEM exhibited a slight increase in PSNR when using these augmented labels. To further unleash the potential of the second-stage DNN, we can leverage Masked Image Modelling (He et al., 2022; Huang et al., 2023a) for pre-training, which we leave for future work. For consistency, these augmentation strategies were not applied in other experiments.